# Post Access Report

Advanced PTO Control Strategies for the Triton-C WEC

Awardee: Oscilla Power Inc.
Awardee point of contact: Tim Mundon
Facility: Sandia National Laboratories
Facility point of contact: Dominic Forbush

Originally submitted: 2/8/2023
Revised with comments addressed: 11/03/2026

## Executive Summary

The overall objective of this work was to increase power performance from the Triton-C WEC through the addition of advanced (active) PTO control, with the goal of significantly reducing the cost of energy from this system. Controllers were developed and evaluated using numerical representations of the Triton-C, including reduced order linear models and a coupled hydrodynamic and component-level PTO model. Refinement using experimental data and evaluation during a full-scale ocean deployment were planned, but were not completed during this activity because at-sea testing was delayed. These remain future steps towards establishing the effect of the developed strategies on the Triton-C's AEP.

The Triton-C device was modeled at 3 levels of fidelity, and diagonal proportional, proportional integral, and cross-coupled proportional controllers were evaluated. Electrical power maximizing gains were identified in each case through brute-force mapping of the power surfaces as a function of the controller parameters. In the vicinity of these gains, the effect of controller parameter selection on cable loads were also considered. While the lower fidelity models of the Triton-C device were useful in some cases, they do not always develop characteristically similar power surfaces and thus controllers suggested by lower fidelity tools should be checked against the best-available device model to ensure validity. Beyond identification of an optimal diagonal damping controller, minimal power gains were observed for PI and cross-coupled proportional control, with the latter showing a 2% performance increase in 2 of the 3 tested sea states. Controller gain selection strongly affects cable load, and though controller optima are not coincident with the maxima of load variance, sub-optimal controller gain selection can significantly reduce cable load variance, if desired. Significant work was needed to ensure that the coupled hydrodynamic and PTO model could run stably in the investigated sea-states and controller configuration, and will be useful for any future work in the space.

# 1 Introduction to the project

Through TEAMER, OPI worked with Sandia National Laboratories (SNL) to develop advanced PTO control strategies for the Triton-C with the aim of achieving meaningful performance increases. Algorithms were investigated that aim to maximize power capture in small to moderate wave conditions where most of the AEP is realized. Importantly, strategies were developed and evaluated with an eye towards real irregular seas. Due to the challenges in wave-by-wave forecasting in real seas, this project focused primarily on causal strategies. To accomplish this objective, Sandia used frequency-domain models, linear identified system models, and component-level simulations of the Triton-C to design multi-input, multi-output (MIMO) causal feedback controllers. The models were intended, at different stages in the work, to be based on BEM, linearization of nonlinear numerical models (e.g. OrcaFlex, CFD), or system identification of wave tank or at-sea test data, but not all of these data sets were available over project duration. The control strategies developed can potentially incorporate some self-tuning capability to allow the controller to automatically adjust gains to suit the prevalent sea state.

OPI provided numerical hydrodynamic results and a detailed PTO model, which Sandia used to develop and evaluate the controllers described in this report. Implementation of the best performing algorithms on the Triton-C during deployment at WETS remains future work. An at-sea comparison of AEP against OPI's baseline passive control strategy was therefore not completed during this activity.

Most of the literature on active control has focused on single-body point-absorber type WECs that use the seafloor as a reference, and existing work in the field has illustrated that significant performance increases can be achieved. The application of active control to two-body, self-referenced WECs has received some attention, but given the additional complexity of a two-body system, this problem has received less treatment. Some references (Ringwood et al., IEEE, 2014) suggest that mild performance increases can be achieved with this architecture, however significant uncertainty about the achievable performance gains remains. Multi-mode variations of two-body systems such as the Triton add another level of complexity to the problem and to date have not yet received any treatment in the literature.

OPI have completed some preliminary investigations to identify a rough magnitude of the PTO requirements for advanced controls in the Triton-C. These were taken into account during the design and construction of the Triton-C such that it may be used as a platform for this type of investigation.

# 2 Roles and Responsibilities of Project Participants

## 2.1 Applicant Responsibilities and Tasks Performed

OPI performed in-house numerical 'tank tests' of the Triton-C system. Under guidance from Sandia, OPI executed forced oscillation and wave excitation simulations to support the extraction of reduced-order linear representations for control design. OPI also provided the detailed component-level PTO model. Implementation of the developed algorithms on Triton-C hardware and subsequent at-sea testing were planned responsibilities that were not completed during this activity.

### 2.2 Network Facility Responsibilities and Tasks Performed

Sandia led linear modeling and control design efforts. Sandia drew on experience and knowledge developed in the Advanced WEC Dynamics and Controls project and a diverse set of expertise, spanning from naval architecture, controls, electronics, robotics, and aerospace engineering. Sandia has developed an engineering approach to WEC modeling, testing, and control design [1–6], and drew on these methods in their collaboration with Oscilla.

## 3 Project Objectives

The ability to increase power performance from the Triton-C system through the addition of advanced (active) PTO control is an important way to increase AEP. This can make a significant reduction to the cost of energy from this system. It is also expected that the learnings from the development of control for the Triton-C could be applied to other WECs based on the Triton architecture and potentially, more broadly, to multi-body multi-mode WECs in general.

The original test plan established the following performance objectives for evaluation using OPI's numerical models of the Triton-C:

- Mean power in a given sea state: Compare advanced causal control against OPI's baseline passive control strategy in representative sea states, with a target mean power improvement of 20%.
- Reactive power requirements: Keep peak reactive power within the peak power capability of the OPI drivetrain, which was oversized for this purpose.
- Peak tendon loads: Use peak tendon loads as a proxy for reliability, with a target increase of no more than 20% relative to passive control in a comparable sea state.

The completed numerical investigation compared controller power capture in three sea states and examined cable load variance and generator saturation. In the full model, cross-coupled proportional control provided a 2% improvement over optimized diagonal control in two sea states; this comparison does not establish a 20% improvement over OPI's original baseline. The reported load variance and saturation results likewise do not establish compliance with the original peak tendon load and peak reactive power targets. Evaluation of these metrics on the ocean-deployed Triton-C remains future work.

## 4 Test Facility, Equipment, Software, and Technical Expertise

- Physical equipment, hardware, and instrumentation - N/A; this activity comprised numerical analysis.
- Simulation or data analysis software utilized - This project relied primarily on MATLAB, Simulink, and Simscape. Sandia tools, including `fbWecCntrl`[1] and `WecOptTool`[2] informed the planned approach. However, the system nonlinearities prevented direct use of established workflows such as *WecOptTool*.

[1] `https://github.com/SNL-WaterPower/fbWecCntrl`
[2] `https://snl-waterpower.github.io/WecOptTool/`

- Critical personnel expertise utilized to achieve the project objectives
  - **Giorgio Bacelli:** Dr. Giorgio Bacelli is a senior research engineer in the Water Power Technologies group at Sandia National Labs. He received his master's degree form Università Politecnica delle Marche and his PhD from the National University of Ireland, Maynooth. He has more than 10 years of experience in wave energy conversion, in the areas of WECs dynamic modeling and control. He has experience also in experimental testing, including sensors and actuation design, design of experiment and data processing (system identification), in the fields of wave tank testing and plasma processing.
  - **Ryan Coe:** Dr. Ryan Coe is a principal research engineer in the Water Power Technologies group at Sandia National Labs. He has expertise in computational methods, hydrodynamics modeling, and wave tank testing. Ryan also has experience and training in naval architecture, ship design, and ocean engineering. Ryan has a bachelor's degree in ocean engineering and a PhD in aerospace engineering from Virginia Tech.
  - **Dominic Forbush:** Dr. Dominic Forbush is a post-doctoral appointee in the Water Power Technologies Program at Sandia National Laboratories. Dominic's research focuses on the control, modeling, and the development of innovative solutions for wave energy convertors (WECs). Particularly, Dominic is involved in developing and supporting open-source WEC modeling tools, wave tank testing of WEC devices and control approaches, and the application structured innovation techniques to the wave energy space. Dominic has a bachelor's, master's, and doctorate all in mechanical engineering from the University of Washington, where his graduate work focused on the control of cross-flow hydrokinetic turbines.
  - **Steven Spencer:** Dr. Steven Spencer is a senior research engineer in the High Consequence Automation and Robotics group at Sandia National Laboratories. He received a B.S. in Mechanical Engineering from University of Maryland, and an M.S. and Ph.D. in Mechanical and Aerospace Engineering from University of California, Irvine. His research interests include design and control of energy efficient robotic systems. He has been collaborating with the Water Power Technologies group on the design and control of WECs for the past two years.
- Ocean test site conditions and equipment needed to accomplish the testing: the Triton-C is equipped with a Speedgoat real-time controller intended to implement the developed control strategies during a future WETS deployment. Hardware implementation and at-sea evaluation were not completed during this activity.

## 5 Test or Analysis Article Description

Oscilla Power (OPI) is developing the Triton wave energy converter architecture. This system is a two body, multi-mode point absorber consisting of a surface float connected to a submerged ring via three tendons. As the surface float is articulated by waves, the two bodies react against each other in all modes of motion to capture mechanical power. The resulting power, in the form of tension and displacement variations in each tendon, is transmitted to three independent power take-offs (PTO's) housed inside the surface float, one per tendon. The system has the ability to submerge in extreme waves to mitigate storm loadings, a strategy that has been validated both numerally and in physical experiments. OPI is developing

different WEC variants based on the Triton architecture that share these core operating principles. At present there are two variants, the Triton (MW, Utility scale variant) and the Triton-C (100kW variant), which are differentiated by their physical size and drivetrain design. The Triton has a linear input driving a hydraulic power conversion system, while the Triton-C has a rotary input driving an electrical conversion system.

The two variants of the Triton system are targeted at different markets. The utility-scale Triton is a 1MW rated system that is intended to be installed in large arrays to produce significant quantities of grid-scale power. It is optimized for long term reliability and minimum operational expenditure over its lifetime. OPI anticipates that this system will result in a competitive and attractive LCOE when installed in quantity.

The Triton-C variant is a 100kW community-scale wave energy converter that is intended to provide energy to remote, isolated or tribal communities globally. It is intended to be installed individually or in small numbers. Potentially the Triton-C is able to provide power for persistent marine operations.

While the cost of energy for the Triton-C is expected to be higher than that produced by the Triton (MW-Variant) it is still expected to be an attractive, cost-effective option for isolated remote locations that currently rely on diesel generation.

# 6 Work Plan

## 6.1 Numerical Model Description

Mid-fidelity models of the Triton and Triton-C systems have been developed using the commercial hydrodynamic codes Orcina OrcaFlex and DSA's ProteusDS. These codes solve for the multibody dynamics of the coupled marine and PTO system, using the hydrodynamics derived from a frequency domain boundary element method (BEM) solver and nonlinear viscous terms accounted for through Morison-type elements. The Triton model has been extensively validated from the Wave Energy Prize tests and subsequent 1:30 physical model tests. The Triton-C (variant) model, specifically, has been validated from 1:10 physical model tests through the MARINET program, and OPI have been able to confirm power prediction accuracy to within 10%.

At the most basic level the Triton/Triton-C drivetrain consists of a spring, to support the mean reaction ring load, and a damper (generator) to provide the power take off. Work we have performed in collaboration with the University of Washington (supported through NAVFAC) suggests that latching control applied to two-body flexibly connected WECs is likely to lead to only small gains in power performance. However, more complex spring-damping control, in which the generator also provides reactive power (such as a simulated spring component), may provide more significant increases in power capture.

OPIs current controls strategy is based around optimum passive control and is limited to using a linear damping profile that is the same for each of the Triton/Triton-C generators and that acts in parallel with the hydraulic return spring. This project investigated a more generalized (reactive) control strategy where each of the generators have independent tuning parameters (spring, damping) based on its own motion as well as on the motion of the other two generators.

Based on the OrcaFlex results, linear hydrodynamic models were developed and fitted via system identification (SID) methods (see, e.g., [7]). These models were coupled with representations of the PTO to perform control design.

Table 1: Summary of project activities and completion status.

| **Activity** | **Actual work and status** |
|---|---|
| Hydrodynamic identification | Completed using OrcaFlex multi-sine and wave excitation simulations to identify admittance and excitation models. |
| PTO identification | Completed over multiple excitation amplitudes; linear approximations required a separate friction model and retained limitations. |
| Closed-loop modeling | Completed at three levels of fidelity, with substantial modifications to stabilize the coupled hydrodynamic and PTO simulation. |
| Control evaluation | Completed for SS1, SS2, and SS3 (Table 5), including proportional, PI, and cross-coupled proportional control investigations. |
| At-sea model updates and control evaluation | Not completed during this activity because deployment and at-sea testing were delayed. |
| Reporting | Numerical methods, results, and limitations are documented in this Post Access Report. |

### 6.2 Test and Analysis Matrix and Schedule

A range of simulations was conducted to identify hydrodynamic and PTO models and evaluate closed-loop controller performance. The original plan called for PTO identification at three fractions of rated torque. Strong nonlinearities at both small and large amplitudes required a more refined set of identification cases and explicit treatment of pump friction. Table 1 summarizes the completed numerical activities and the planned activity that was not completed.

The original schedule allowed six months, with system identification in Month 1, initial and revised closed-loop simulations in Months 2 and 3, at-sea testing in Month 5, and reporting in Month 6. The project was extended because development of a stable closed-loop model required substantially more effort than anticipated. The completed work progressed from system identification through model stabilization and controller evaluation to reporting.

### 6.3 Safety

N/A - this is a numerical analysis project

### 6.4 Contingency Plans

As discussed in Section 6.2, the assessment of system nonlinearity showed that local linear PTO models alone were not sufficient. A separate friction approximation and a detailed PTO model were therefore retained for the controller investigations.

The numerical investigation was completed without ocean deployment data. At-sea testing was delayed, so validation of the developed algorithms on the physical system and model refinement using deployment data remain future work.

Table 2: Signals identified in the original data management plan for submission to MHK-DR.

| Signal | Description |
|---|---|
| Generator torque | Time-series in key sea states. Baseline and Advanced control |
| Generator power | Time-series in key sea states. Baseline and Advanced control |
| Tendon tension | Time-series in key sea states. Baseline and Advanced control |
| Generator displacement | Time-series in key sea states. Baseline and Advanced control |
| Generator velocity | Time-series in key sea states. Baseline and Advanced control |

### 6.5 Data Management, Processing, and Analysis

#### 6.5.1 Data Management

Oscilla's Dropbox was used as the designated project data storage location. Table 2 summarizes the signals identified in the original data management plan for submission to MHK-DR. The work reported here comprised numerical modeling and controller evaluation.

#### 6.5.2 Data analysis & Processing

Data analysis for SID followed the methods demonstrated in [7]. Linear hydrodynamic models were created from the OrcaFlex results (Section 6.1), and PTO models were identified from the component-level simulation. System nonlinearity was assessed over multiple excitation amplitudes, and controller performance was evaluated in three sea states. The approaches described in [1, 2] informed control development, but the nonlinear PTO behavior required the model modifications and numerical gain searches described below. Model updates based on ocean deployment experiments were not completed.

## 7 Project Outcomes

### 7.1 Results

#### 7.1.1 System Identification

OPI performed diffraction and excitation simulations using an ORCAFLEX model of the wave-interacting components of the Triton-C. These tests were carried out according to the system identification approach of [7], using broad-banded multi-sine excitation signals on each degree of freedom to determine the intrinsic impedance of the device. Separately, OPI provided a detailed PTO model in Simscape. This model takes as an input the force exerted on each PTO tether. In order to meaningfully pursue controller development, it is necessary to create combined model of hydrodynamics and PTO capturing all relevant dynamics. To this end, three separate system identifications were attempted.

1. 3 x 3 (3 input, 3 output) system calculating the tether velocity (m/s) from the force (N) applied to each of the tethers from the ORCAFLEX (OF) model, $Y$ (Figure 1).
2. 1 x 3 system calculating the tether force (N) from wave elevation (m), again using the ORCAFLEX (OF) model, $H$ (Figure 2).
3. 3 x 3 system calculating the tether force (N) from the generator torque command (N-m) from the detailed PTO model (SL), $G_o$ (Figure 3).

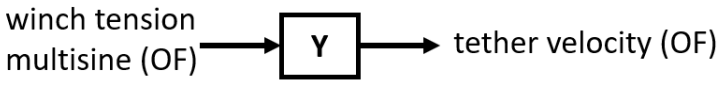



Figure 1: The open-loop model used to identify $Y$ from ORCAFLEX (OF) data.

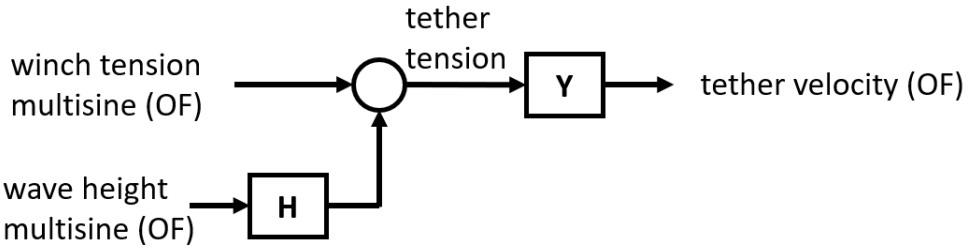



Figure 2: The open-loop model used to identify $H$ from ORCAFLEX (OF) data after $Y$ has been identified.

In a typical procedure, the objective of each system identification would be to fit a transfer function to the identified system so that it can be used directly in a time-domain Simulink model for both open loop and closed-loop simulations. In this way, tether force becomes a common output from the PTO and excitation models, which can then used to estimate tether velocity, which acts as an input to the controller $C$ to be studied.

However, as will be shown, it was not possible to adequately approximate $G_o$ with a linear, or a family of linear models due to a strong non-linearities at both large and small amplitudes of motion. This forced a revised approach to be considered in which a 6 input (three prescribing tether velocities, three prescribing generator torque applications) and 3 output (force measurements at each tether) model $G$ was constructed that *excluded* the pump losses near zero velocity that resemble static friction (see Section 7.2, Figure 4). The time-domain approximation of system dynamics based upon these linear models must then include this static friction model to be reasonably accurate. This is undesirable as it limits the extent to which optimal control parameters can be derived analytically, but is necessary in this case because the particular dynamics of the detailed PTO model strongly affects control decisions.

### 7.1.2 Expanding electrical model

The provided PTO model essentially treated the generator as a scheduled damper, and did not resolve the dynamics or losses of the device. These effects were included through the electrical model development described below to support electrical power calculations. Specifications provided by OPI are summarized in Table 3, in which an asterisk indicates a value that was calculated or tuned from OPI provided parameters.

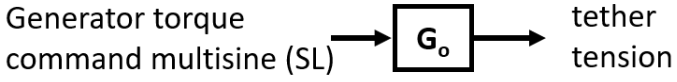



Figure 3: The open-loop model used to identify $G_o$ from the Simulink (SL) detailed PTO model.

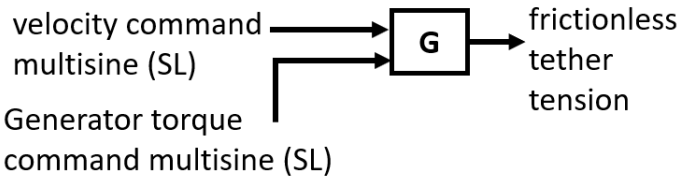



Figure 4: The open-loop model used to identify $G$ from the Simulink (SL) detailed PTO model.

Table 3: OPI-provided generator and drive information used in Simulink

| **Parameter** | **Value** | **Variable** |
|---|---|---|
| Winding Resistance | 0.0215 (Ohm) | $R_s$ |
| Field Inductance | 0.55 (mH) | $L_d$ and $L_q$ |
| Number of Poles | 16 | $N$ |
| Number of Phases | 3 | (n/a) |
| Torque constant (nominal) | 7.1 (Nm/A) | $K_t$ |
| Permanent magnet flux linkage* | 0.5917 (Nm/A) | $PM$ |
| Torque time constant* | 0.0005 (s) | (n/a) |

Permanent magnet flux linkage was calculated as

$$PM = \frac{2K_t}{3N}$$

.
Additionally, a plot of drive efficiency was provided. Using visual estimates from this image (see Appendix), a drive efficiency surface was constructed (Figure 5).

While it is possible to implement this motor/generator directly into the PTO model, the relatively high-frequency of the detailed electrical dynamics results in a highly stiff system that creates both stability issues for Simscape solvers and excessive simulation run times. These high-frequency dynamics were not found to significantly affect the outputs of interest. With this in mind, the torque command response time of a simpler motor and drive model block was tuned to the provided motor dynamics to yield a similar response to torque commands under identical inertial loads for a square wave of various frequencies (10 Hz max) and an amplitude of 1000 N-m (Figures 6 and 7).

### 7.1.3 ORCAFLEX Hydrodynamic Impedance Identification

Following the procedure of [7], distinct phase realizations (three in total, denoted A,B, and C) of a multi-sine excitation signal from 1/30 to 1/2 Hz was supplied as a tension command to each winch. This was repeated 3 times, so that three independent data sets were available to solve for the 3 x 3 frequency domain admittance model, $Y$, relating the input tether tension (N) to output tether velocity (m/s). These non-parametric models were then fitted with a parametric sixth order transfer function. (Figure 8).

The starboard and port identified system are nearly identical in amplitude and phase, which is intuitive from device geometry. Bow response is unique with two distinct resonance peaks (typical for 2-body relative motion) and generally larger amplitude. The model is nearly symmetric about the diagonal. All elements are well approximated by the transfer function (Figure 9).

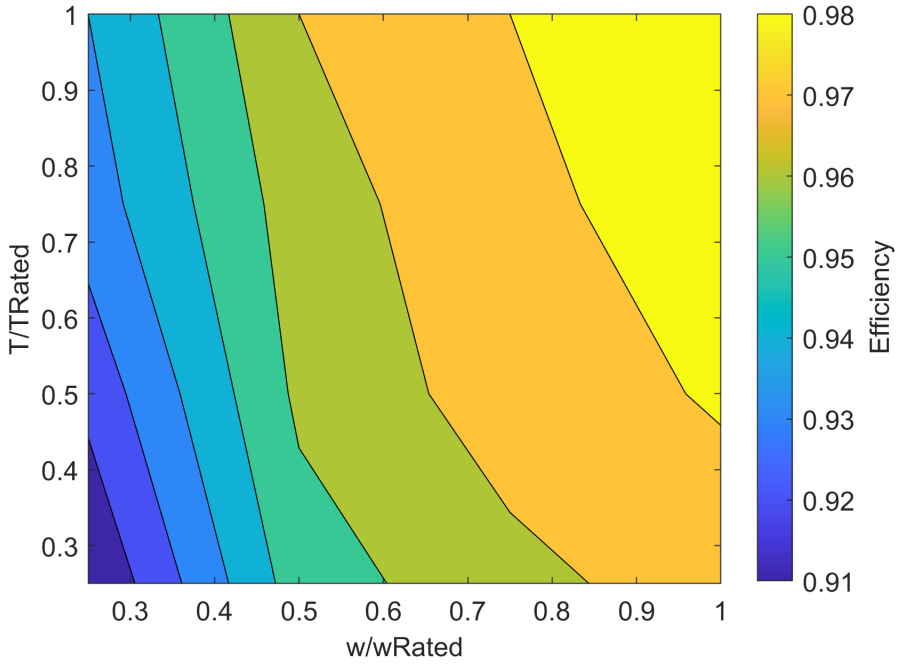



Figure 5: Drive efficiency map as a function of torque and velocity.

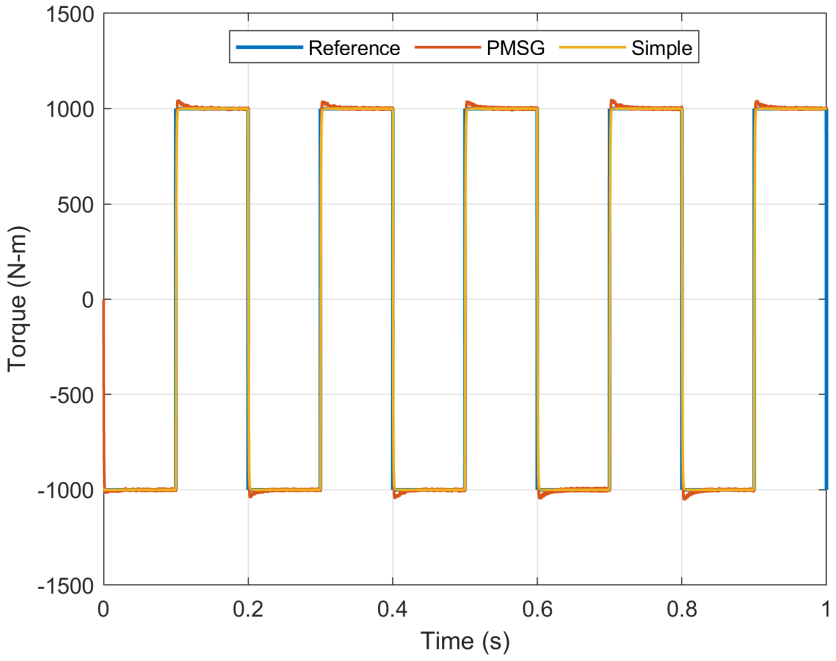



Figure 6: Tuning the simple drive implementation to the PMSG torque response for a 5 Hz, 1000 N-m amplitude square wave.

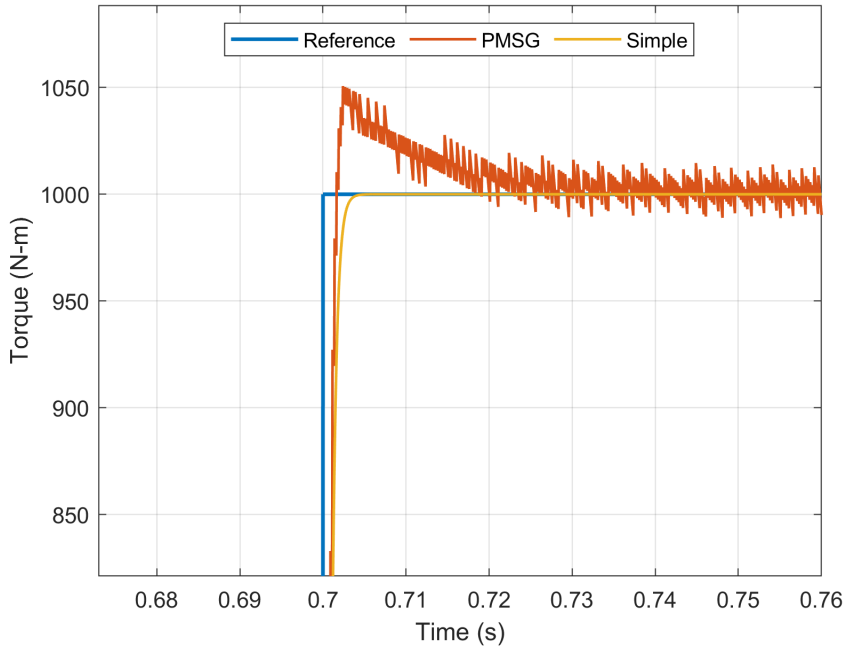



Figure 7: Detail view of tuning the simple drive implementation to the PMSG torque response for a 5 Hz, 1000 N-m amplitude square wave.

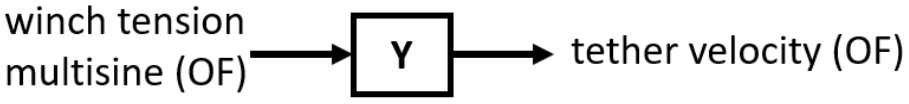
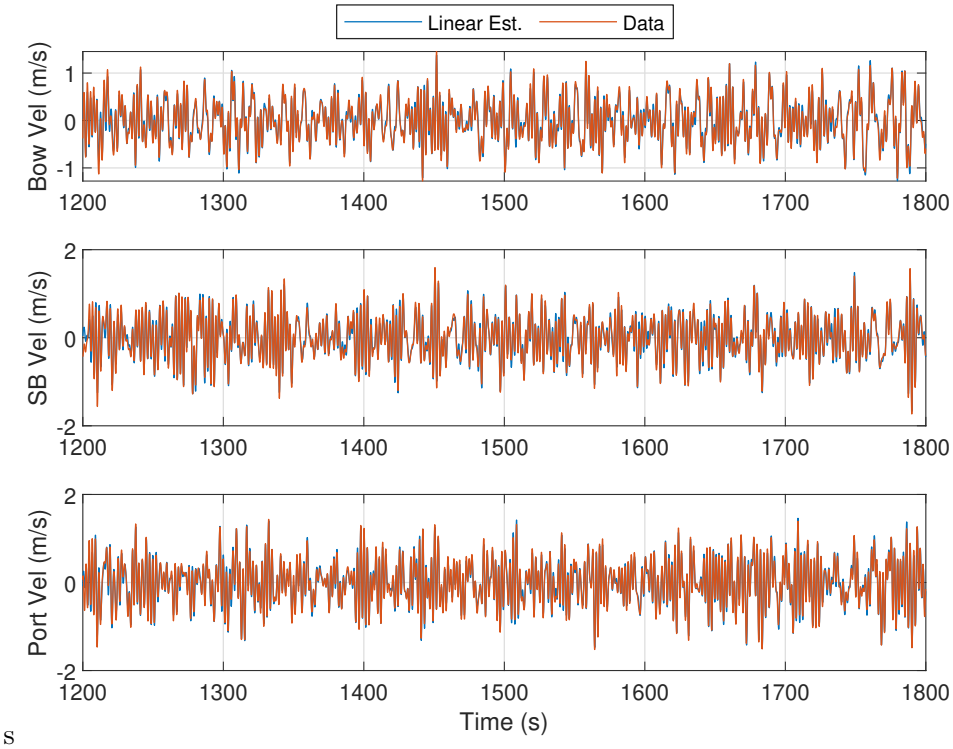



Figure 8: Identified admittance model from ORCAFLEX.




s

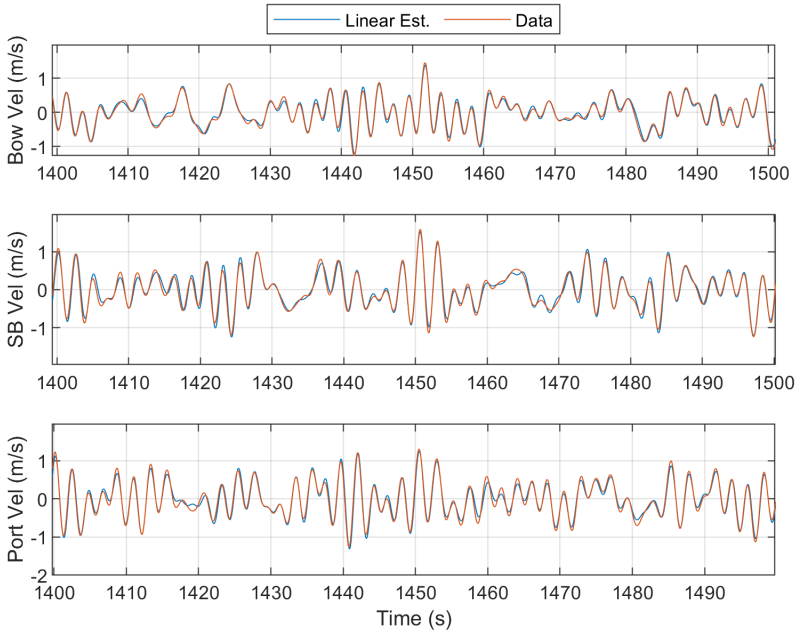



Figure 9: A time-domain comparison of the ORCAFLEX output with the linear system approximation. A detail view is also given.

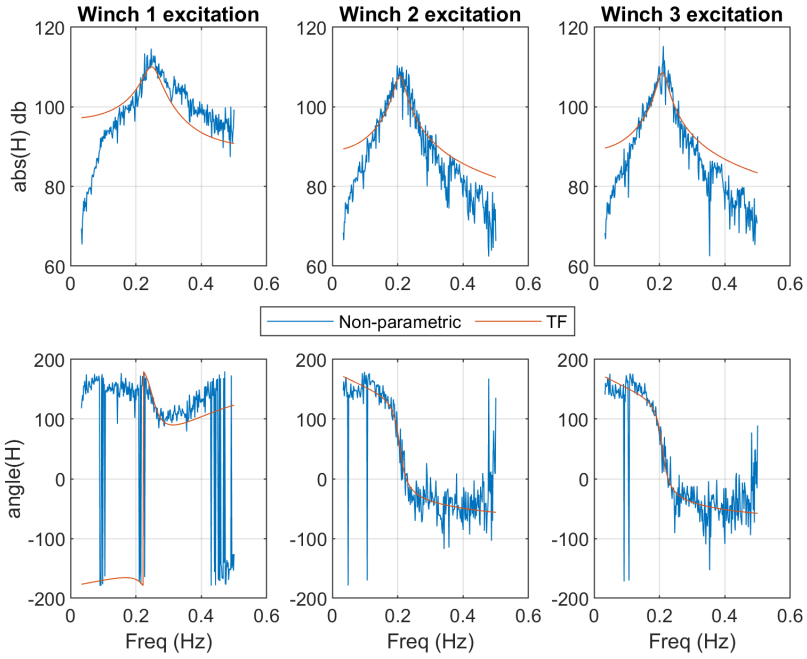



Figure 10: Excitation admittance model identified from ORCAFLEX Runs.

Secondly, this procedure was repeated with the addition of three distinct phase realizations of pink-spectrum waves (i.e., nine runs in total). Using the identified model of $Y$, the contribution of wave excitation to tether load was separated from the total measured, and a wave excitation model was calculated

$$F_{exc} = \frac{V}{Y} - L \tag{1}$$

where $F_{exc}$ is the component of the total tether load $L$ due to wave action and $V$ is the tether velocity, and the division here implies a matrix inverse. From this, $H$ can be calculated

$$H = F_{exc}/\eta \tag{2}$$

where $\eta$ is the wave spectra. This was fitted with a second-order transfer function (Figure 10).

Note that in all cases, it is possible to pre-calculate the time-resolved wave excitation force from a defined wave spectra or wave height time series using the frequency response function directly: the parametric transfer function fit $H$ is included to facilitate future linear modeling, but is not utilized to generate any of the forthcoming results.

The hydrodynamic impedance and excitation models are well-approximated by linear transfer functions. This suggests that, should there be a desire in the future, the device could be more easily modeled as a coupled hydrodynamics-PTO model in WEC-Sim, rather than this disjointed approach.

### 7.2 Feedback Model Stabilization

The complexity of the PTO model, the significant static friction at the pumps, and the necessary means of coupling the (force-to-velocity) admittance model to the Simscape physical

network led to stability issues and non-physical results in the feedback model. The following simplifications were made to produce a stable simulation.

1. Parallel pipe networks were reduced to a single equivalent.
2. Parallel high-pressure accumulators were reduced to a single equivalent.
3. Parallel pumps were reduced to a single equivalent.
4. Pump losses near zero velocity were approximated with a torque deadband.
5. Electric and hydraulic motor inertias were omitted

To verify the validity these decisions, a comparison of the through-variables (flow-rate) were conducted for the PTO Model identification runs. Because of the parallel configuration, the across-variable (pressure) is maintained (though the specifics of the control volume for which this is true varies: for instance, the parallel high pressure pipe-pump-low pressure pipe sections have a common pressure difference between the ends of the HP and LP pipes, though the distribution of this pressure difference at each component can differ). To reduce parallel pipe sections, the Simscape pressure loss model using the Darcy formulation

$$h_f = f\frac{L}{d}\frac{V^2}{2g} \tag{3}$$

where $h_f$ is the pressure loss (as head, units of length), $f$ is the Darcy friction factor, $L$ is the pipe length (m), $d$ is pipe diameter, $V$ is the flow velocity (m/s), and $g$ is gravitational acceleration (m/s$^2$). In terms of flow rate through a circular pipe, this can be expanded as

$$h_f = f\frac{L}{d}\frac{(\frac{q_p}{\pi d^2/4})^2}{2g} \tag{4}$$

where $q$ is the volumetric flow rate through the pipe. For simplifying the pipe network, $h_f$ is maintained as the across-variable. The pipe material is maintained, $f$ is constant. To maintain total flow rate across the network, we define the equivalent flow $q_{eq}$ as the sum of the constituents

$$q_{eq} = \sum_{1}^{n} q_{pn} \tag{5}$$

Assuming equal flow rates through the parallel network (a good assumption in 1) and 2), reasonable in 3)) equal to the average of the constituent flows, this simplifies further to

$$q_{eq} = 5q_{av} \tag{6}$$

Finally, substituting this result into Eq. 4

$$h_{eq} = f\frac{L_{eq}}{d_{eq}}\frac{\frac{q_{eq}}{\pi d_{eq}^2/4}}{2g} \tag{7}$$

we can set $h_{eq}$ equal to $h_f$, ensuring the network pressure drop is maintained and canceling equivalent terms we have 2 potential parameters that can be modified to define an equivalent single pipe section, diameter $d$ and length $L$. For convenience, $d$ was maintained (in all cases, parallel pipes have identical diameters), and $L_{eq}$ was calculated to maintain equivalent flow rate as

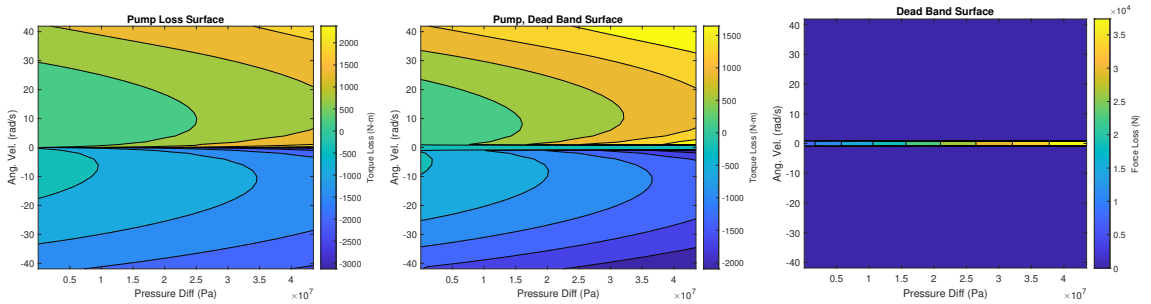



Figure 11: Total loss table (left) and the decomposition of this table into pump losses (middle) and those utilized at the dead-band (right).

$$L_{eq} = L/n^2 \tag{8}$$

where $n$ is the number of parallel constituents. If this approach of maintaining total flow rate and pressure drop during simplification is expanded to the parallel pumps, it implies that the equivalent pump displacement is $n$ times the individual pump displacement and, because parallel pumps are on a common shaft, the equivalent mechanical loss is $n$ times the individual mechanical loss (assuming equivalent pressure differences). Similarly, the equivalent high-pressure piston accumulator area and dead volume are $n$ times the individual accumulator parameters.

This reduction method depends on the average flow rate in each parallel pipe $q_{pn}$ being equivalent: this is not perfectly true under all simulated conditions, but by inspection of the PTO Model identification runs, this is a very good assumption for items 1) and 2), and a reasonable assumption for item 3). Because these parallel pumps are coupled to a common shaft, their angular velocities are identical, and it is their aggregate torques contributing to power capture, the ultimate figure of merit, it is unlikely that this will have a significant impact on the power results. Additionally, the reduction of the parallel pump network was necessary to deal with the static friction via the dead-band approximation.

The single largest contribution to the difficulty of a feedback model involves the coupling of the hydrodynamic admittance $Y$ with the detailed PTO model. Primarily, $Y$ requires an input of a total force on the cable, which is the sum of the PTO-exerted force and wave excitation, to prescribe a cable velocity that takes into account the hydrodynamics identified in the ORCAFLEX model. Practically, this acts as a linear velocity source to the sheave. The PTO-exerted force is measured at the same location. A linear model, $Y$ cannot directly account for the effect of static friction: a non-zero prescribed force implies a non-zero velocity. Because the velocity source acts ideally (i.e., it can provide whatever force is necessary to achieve the prescribed velocity), in the case that the measured force is inadequate to overcome static friction such that the sheave velocity should be zero, the velocity enforced by the ideal velocity source will be non-physical. This implies that the force input to the admittance model must be modified to account for static friction.

To achieve this, the pump loss table was decomposed into two sections: near zero velocity, where sharp increases in pump mechanical losses act like static friction, and far from zero velocity, where there may be significant power capture. A threshold value of 0.1 rad/s at the pump (i.e. 0.0152 rad/s at the sheave, 0.289 rad/s at the generator) was selected (Figure 11).

A variable dead-band is implemented on the total force input to the admittance model (Figure 12). Because the dead-band is applied to the linear force input to the cable, the torque loss is converted to the linear force, using the pump gear ratio and the sheave radius

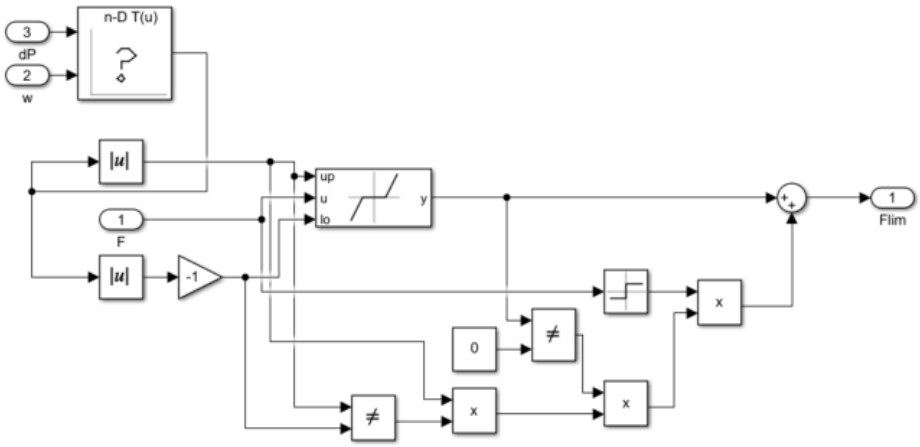



Figure 12: The dead-band logic on the total force input to the admittance model. The logic in the lower right ensures that the dead-band width is added to the total force when the input force exceeds the dead-band, so that the total force (rather than just that in excess of the dead-band) is output to the admittance model when appropriate, and the output force is zero otherwise. However, because this correction is only applicable during the one (or rarely, two) time-step transitions between the logic being high/low, it can be omitted without consequence, and was in later models, but is included here for completeness.

as

$$F_{dead} = T_{dead} N_{pump} / R \tag{9}$$

In this way, when the velocity is nearly zero, the pumps are treated as lossless, with the torque loss approximated by the dead-band. When the velocity is significant, the dead-band is zero, and the pump losses are those originally specified. This allows the accuracy of power calculations (which are only significant when velocity is far from zero) to be retained, but ideal velocity source necessary to the feedback analysis of the model to respect the dynamics imposed by the static friction.

Notably, the torque loss at the pumps modeled in this dead-band approach, amounts to $\sim 30\%$ of the generator rated torque, accounting for the intervening gearbox. It is therefore unsurprising that static friction has a significant dynamic effect.

It was recommended by MathWorks that the inertia of the pump, sheave, and electric motor not be included in the model. When fed by an ideal velocity source, this acts like a highly stiff system because the ideal velocity source exerts whatever force is necessary to achieve the desired velocity. Considering all of the inertia type elements present in the system, the buoy and heave plate static and added masses are likely to far exceed the total inertias (when translated into the common translational frame). This removes significant high-frequency ringing from the simulation: this ringing is likely nonphysical and it is present due to the unrealistically ideal assumptions of perfectly stiff drive-train components coupled with the ideal velocity source necessary for feedback. In short: to model PTO inertias introduces significant computational difficulties while providing little benefit to potential simulation accuracy.

Because these inertias are all rigidly connected, it is also possible to add this inertia into the admittance model. Impedance (the inverse of admittance) can be expressed via manipulation of the frequency-domain Cummins equation.

$$Z_i = i\omega(M + m(\omega)) + B_v + B(\omega) + \frac{S}{i\omega} \tag{10}$$

where $M$ is the static inertia, $m$ is the added inertia, $B_v$ is the linear viscous damping, $B$ is the radiation damping, and $S$ is the hydrostatic stiffness. Thus, transferring the inertia as reported across the gear ratio of sheave radius, the impedance model can be adjusted

$$Z_i = i\omega(M + m(\omega) + I(0.5^2)) + B_v + B(\omega) + \frac{S}{i\omega} \tag{11}$$

where 0.5 is the sheave radius (m) and $I$ represents the generator and pump inertias as exerted on the sheave shaft. However, note that the imaginary part of $Z_i$ is on the order of $1e5$, whereas the PTO inertia as exerted on the cable is 525 kg-m$^2$: there is little benefit in making this modification to the frequency response function since the error associated with transfer function approximation is larger.

### 7.2.1 PTO Model identification

The PTO model is a 6 input system: the velocity input from the admittance model and the torque command on the generator from the controller for each the bow, starboard, and port degrees of freedom. Thus, to identify a model here, it is necessary to force the model open-loop with 6 distinct realizations of multisines (3 for a velocity, and 3 for a torque) and measure the resulting measured force on the cable tether.

The test plan called for PTO identification at three distinct fractions of rated load. However, strong system non-linearities exist at both small and large excitation amplitudes that suggest a more refined set of models are necessary to accurately characterize the system. At small excitation amplitudes, static friction on the five parallel pumps on each drive shaft contributes substantial non-linearity. At large amplitudes, there are frequent saturations of the motor/drive. There is a not a significant range of amplitude over which either of these contributions can be neglected. In fact, even over this highly discretized range, local linear approximations were not found to be adequate. The primary reason appears to be that static friction is extremely significant, and in the frequency domain, this elevates the apparent high-frequency content. Across all locally estimated models, and one global estimate, high frequency content is over-estimated and the dynamics of the detailed PTO model (black) are not well-approximated.

The limited accuracy of this approach prompted the modification outlined in Figure 4, where the static friction contribution is moved externally to the system identification. This is undesirable for the resulting model, as it will exclude strictly linear simulation options, but is necessary to increase accuracy. In the full model, the pump friction dead-band is a function of angular velocity, pump pressure differential, and the tether tension. In this reduced friction model, the pump dead-band is averaged over pump pressure differential so that it becomes a function solely of angular velocity and tether tension so that it can be used directly with outputs from the admittance model (velocity) and PTO model (tension).

The resulting models estimated from all amplitudes of exciting multisines is shown as Figure 13. At low frequencies, the diagonal components of the torque-input side of the models resemble gear ratios, with the effective ratio related to the generator gear ratio and the sheave radius. This is true at nearly all frequencies for $G_{all}$. At higher frequencies, this is no longer true, indicating the compliance of the hydraulic-side of the PTO. The model calculated over all amplitudes, and the diagonal-only version of this model, are also shown.

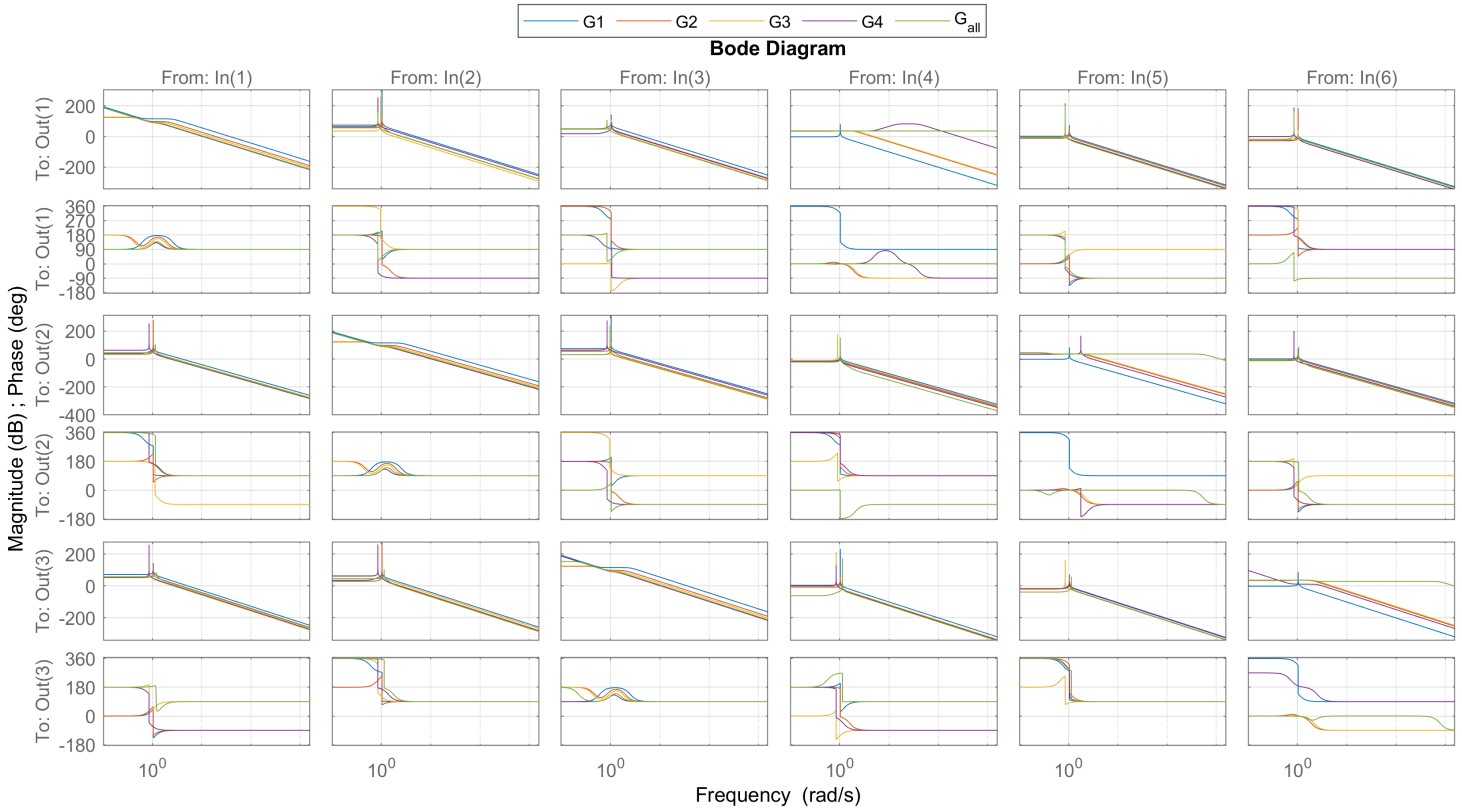



Figure 13: Bode plot of the linear PTO model from all amplitude cases. The "diagonal" model is estimated from all of the amplitude cases, but includes only the diagonal components from each input (i.e., 6 in total). The number associated with $G$ indicates the amplitude of the runs, larger numbers implying larger amplitudes.



SANDIA PROPRIETARY INFORMATION

Table 4: Closed-loop models used for controls investigation

| **Model Name** | **Admittance** | **Excitation** | **PTO** | **Friction** |
|---|---|---|---|---|
| Frequency | Freq. resp. | Freq. resp. | $G$, Torque only | None |
| Linear | TF | Freq. resp. | $G$ | Reduced |
| Full | TF | Freq. resp. | Full | Full |

To validate these models, the output tether tensions from the model used for identification and their estimates from the $G$ models are compared in Figures 14 and 15. Note that not all estimated transfer functions are stable in all cases, and may not appear at the presented interval. To improve stability, the coupling terms between degrees of freedom (i.e., bow torque/velocity inputs affecting starboard and port tether tensions) are removed. This resulting diagonal model presents reasonable accuracy over the amplitudes observed in the three sea-states of interest (intermediate to large) while also being the most stable, although the estimated force on the port DOF is consistently slightly underestimated.

Agreement is poorer in the smallest-amplitude identification case (Figure 14, top). This is an excitation-amplitude case used for PTO identification, rather than a separate operational sea state. At small motions, the near-zero-velocity pump losses are a larger part of the response, and the pressure-averaged friction approximation and linear PTO model cannot reproduce all of these nonlinear effects. This provides a plausible explanation for the discrepancy, although the individual contributions were not isolated. The reasonable agreement at intermediate and large amplitudes should therefore not be extrapolated to low-amplitude conditions; controller predictions in that regime require checking against the detailed PTO model.

### 7.3 Linear Controller Optimization

Three different models were used to study proportional and proportional-integral controller optimizations. These are summarized in Table 4.

In each model, optimal damping and optimal PI controllers were examined. For the 3-DOF system, these are, most generally, 3-input (tether velocity) 3-output (generator torque command) systems, denoted $C$. Thus, the generator torque command (3 x 1) is defined as

$$\tau = CV \tag{12}$$

where $V$ is the line velocity (3 x 1). For damping control, each element of $C$ has the form

$$C(m,n) = K_{p,(m,n)} \tag{13}$$

where $K_p$ is the proportional control gain for the $(m,n)$ index of the matrix. By convention, $K_{p(1,1)}$ contributes to bow control torque by multiplying the bow line velocity, $K_{p(2,2)}$ does the same for starboard, and $K_{p(3,3)}$ for port, with the off-diagonal gains affecting cross-coupling as appropriate. Both diagonal proportional controllers and controllers with cross-coupling terms were investigated.

For a PI controller,

$$C(m,n) = K_{p,(m,n)} + K_{I,(m,n)}/s \tag{14}$$

where $s$ is the Laplace variable, indicating that $K_I$ multiplies the integral of the velocity $V$. The most general control law thus has 18 parameters to optimize, two gains (proportional

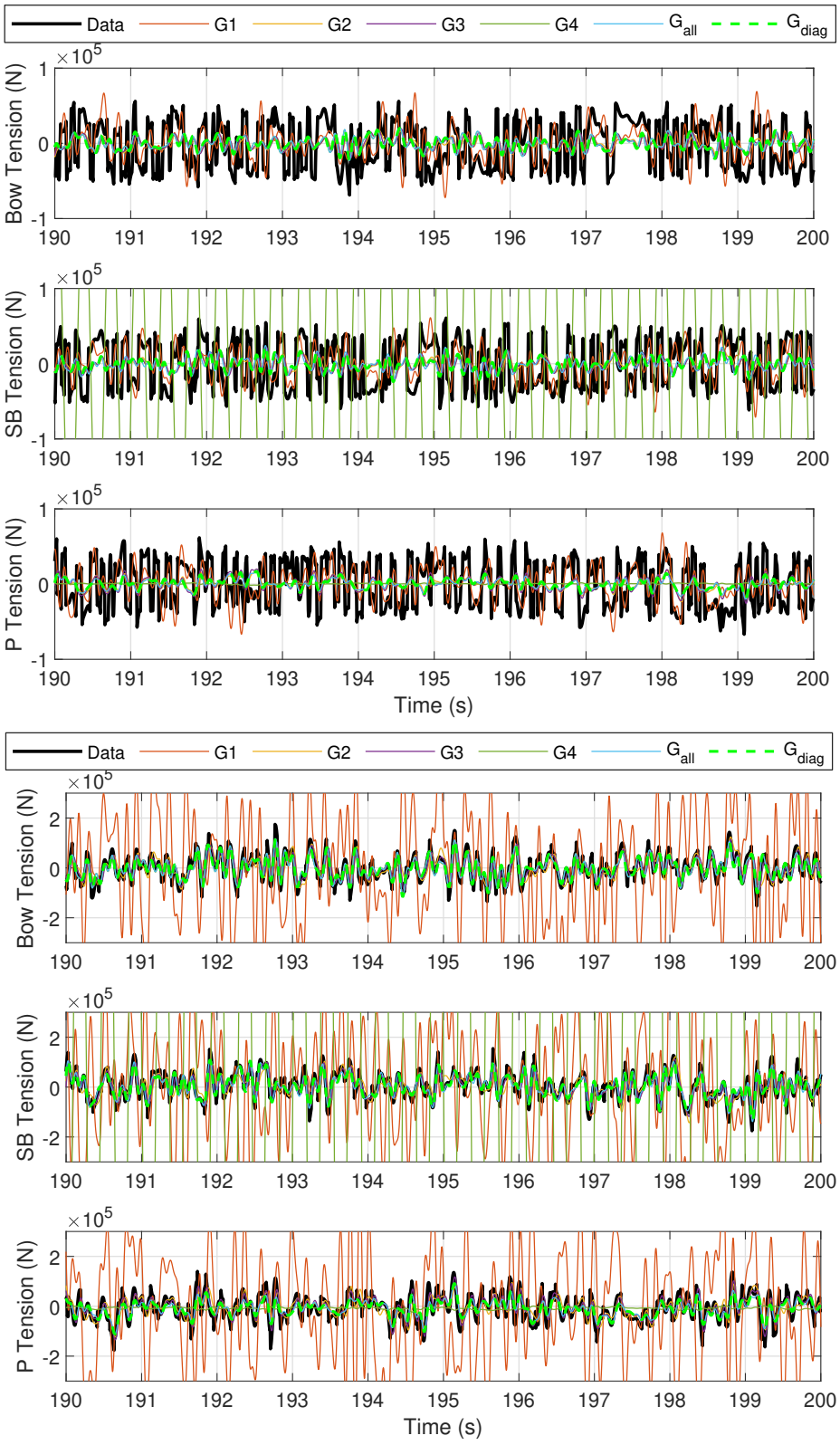



Figure 14: Linear models considered to represent the PTO system for the smallest amplitude case (top), an intermediate amplitude case (bottom). See subsequent figure for high amplitude case.

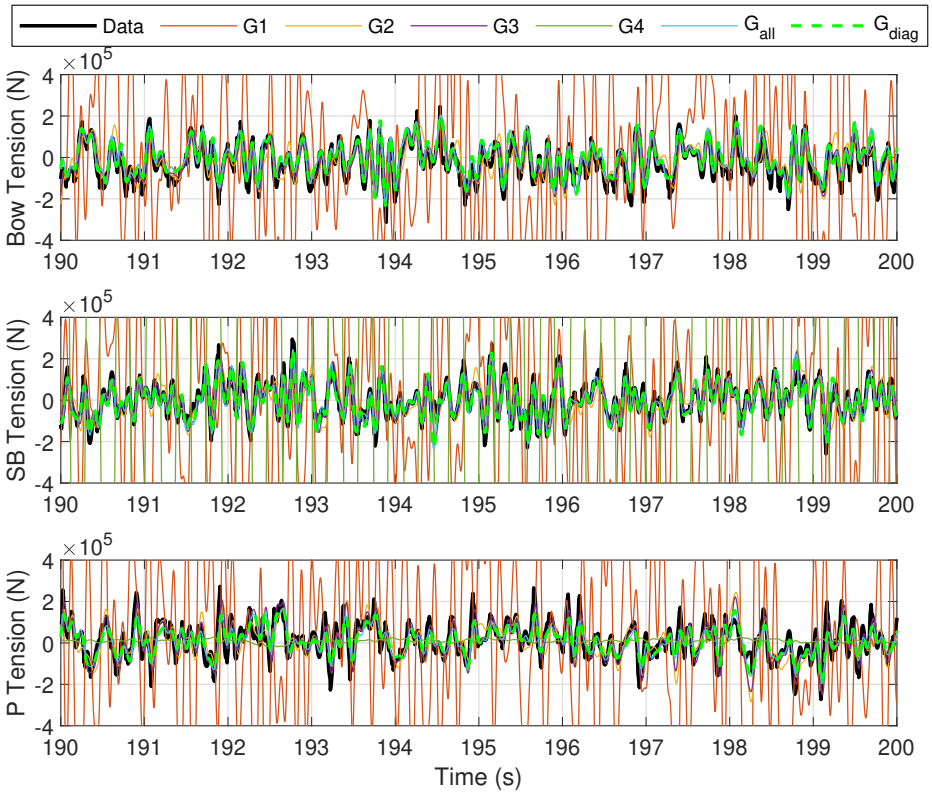



Figure 15: Linear models considered to represent the PTO system for the largest amplitude case. See previous figure for smaller amplitude cases.

Table 5: Operational sea-states of interest

| **Sea-state** | **Significant Wave Height (m)** | **Peak Period (s)** | **Spectra** |
|---|---|---|---|
| SS1 | 3.75 | 12.5 | Bretschneider |
| SS2 | 2.75 | 9.2 | Bretschneider |
| SS3 | 1.75 | 7.7 | Bretschneider |

and integral) for each of the 9 elements of the control matrix. The operational sea-states of interest are specified in Table 5.
Presented surfaces include the average mechanical and electrical powers, along with the variance of tether tensions. Time domain data is available for all of these runs.
Mechanical power is calculated as

$$P_{mech} = \delta t \sum_{i=B}^{P} \sum (\omega_i \tau_i)/T \tag{15}$$

where $\omega$ and $\tau$ are the generator angular velocity (rad/s) and torque (N-m) respectively, and $\delta t$ is the simulation time step, and $T$ is the time over which the calculation is performed. The external summation adds the bow ($B$), starboard ($S$), and port ($P$) degrees of freedom. By sign convention, this implies that power absorbed by the PTO (i.e., the desirable power) is negative. Electrical power lost is calculated as

$$P_{loss} = \delta t \sum_{i=B}^{P} \sum (3R(\tau_i/K_t)^2)/T \tag{16}$$

where $R$ is the generator phase-to-neutral resistance (Ohm) for the 3-phase system and $K_t$ is the generator torque constant (N-m/A). Because this must be positive, the electrical power capture can thus be calculated as

$$P_{elec} = P_{mech} + P_{loss} \tag{17}$$

In the figures, B, S, and P denote the bow, starboard, and port PTOs, respectively; they do not denote rigid-body surge or pitch. KP denotes the proportional gain $K_p$, and KI denotes the integral gain $K_I$. Thus, BKP is $K_{p,(1,1)}$, SKP is $K_{p,(2,2)}$, and PKP is $K_{p,(3,3)}$. BKI, SKI, and PKI denote the corresponding integral gains. Where starboard and port gains are constrained to be equal, SPKP and SPKI denote their common values. A CC suffix denotes a cross-coupling gain between the indicated PTOs, as described below.

For diagonal proportional control, the torque command at each generator is proportional to its own tether velocity, so the proportional gain sets the commanded damping. Here, "optimal damping" means the proportional gain combination giving the largest power capture for the specified model and sea state. These gains have units of N-m/(m/s), because the command is generator torque and the measured input is linear tether velocity; they are not directly a tether-force damping coefficient in N-s/m. The intervening PTO dynamics and gearing determine the corresponding force at the tether. Integral gains have units of N-m/m.

To facilitate visualization in this report, only performance surfaces from diagonal controllers (n=m) are shown for frequency domain models. Additionally, the displayed surfaces represent a slice of a higher-dimensional surface, where the slice is taken at the optimum values in terms of electrical or mechanical power capture (specified per-figure) of the excluded

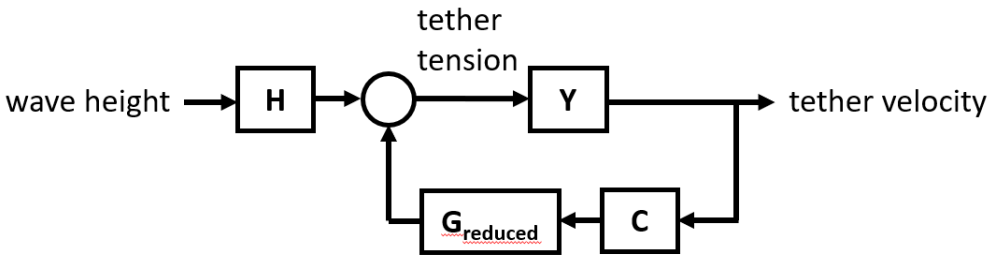



Figure 16: The closed-loop system assumed by the frequency domain model.

Table 6: Frequency-domain model relative electrical power capture

| **Controller** | **SS1** | **SS2** | **SS3** |
|---|---|---|---|
| P, diagonal | 93% | 87% | 89% |
| PI, diagonal | 93% | 93% | 91% |
| PI, symmetric | 99% | 97% | 99% |
| PI, full | 100% | 100% | 100% |

parameters. For example, the surface for a diagonal damping-only controller is 3-dimensional, with one DOF for the bow, starboard, and port control gain. If the surface is presented as a function of the bow and starboard gains, the presented surface is the slice of the 3-D surface taken at the optimum port control gain.

### 7.3.1 Frequency domain model

The frequency domain model is advantageous in that it can directly use the non-parametric frequency domain system identification results rather than relying fitted parametric transfer functions. It can also simulate very quickly, and thus was used for an extensive exploration of the controls space.

It is the least accurate of the models employed for several reasons. Firstly, it does not incorporate any saturation limits or friction models directly, relying on their linearized approximation in $G$ (in the first case) or neglected (in the second case). Secondly, this frequency domain model relies on the state of interest, the velocity of the tether, being defined completely by the sum of the force resulting from the generator torque command and the wave excitation force. As such, only the torque-input side of $G$ can be used in the calculation. Experience with the full, detailed PTO model, indicates that this is not generally true. With that in mind, while we can expect general trends to be captured by the frequency domain model, this is the lowest-confidence method of investigation.

Noting the symmetry of the impedance model, an additional controller that is a middle ground between the strictly-diagonal and the full (18 DOF) controller was attempted. The "symmetric" controller has a symmetric $C$, implying 12 potentially unique control gains.

The power capture results predict significant energy is available through the addition of cross-coupled controller terms (Table 6). This may be a result of the linearization procedure defining $Y$: for small amplitudes, the bow, starboard, and port cross-coupling terms are all generally out-of-phase except at a few frequencies. In reality, if there were significant out-of-phase motion on any single or group of 2 cables, this phase relationship is not likely to be accurate, and as a result, the benefit in power capture for controllers that rely on this cross-coupling relationship is not likely to be as significant as suggested here. Notably, the

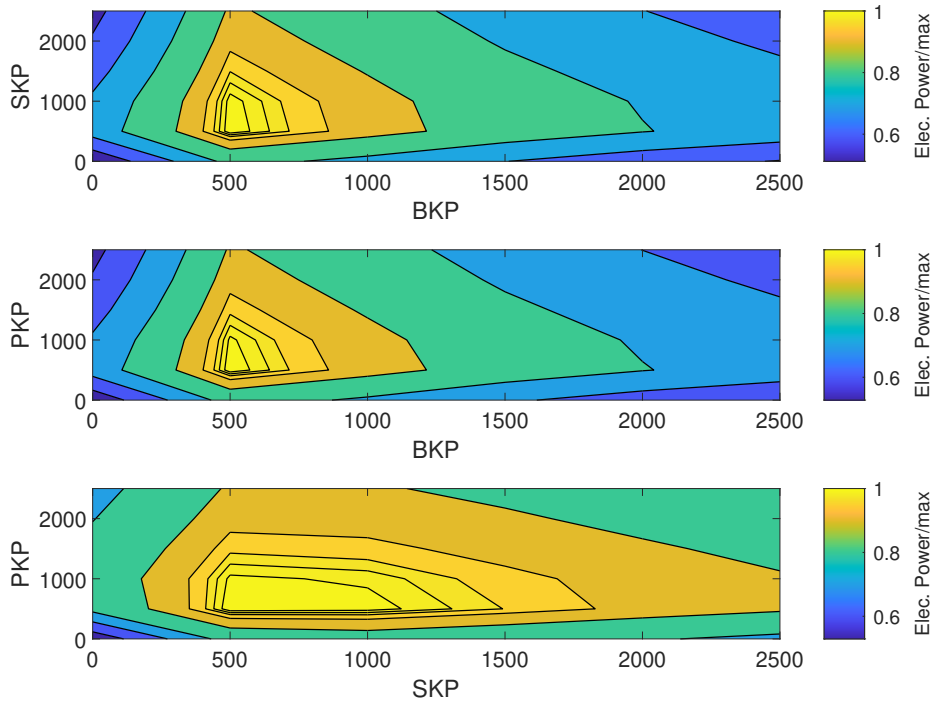



Figure 17: Frequency-domain estimated electrical power for diagonal proportional control for sea-state 1.

symmetric controller performs nearly as well as the full controller in all tested sea-states. Also notable is that optimal damping control is estimated to perform well in these sea-states.

Diagonal controller power capture is shown as a surface in Figures 17 - 22. Figure 17 illustrates how these plots should be read. The upper panel varies the bow proportional gain (BKP) horizontally and the starboard proportional gain (SKP) vertically, while holding the port gain at its optimum. The middle panel varies bow and port gains with starboard fixed, and the lower panel varies starboard and port gains with bow fixed. The color scale gives electrical power capture normalized by its maximum for this case: values near one indicate the best capture, and lower values indicate a reduction. The region near BKP $\simeq$ 500 and starboard and port gains of approximately 1000 therefore identifies a favorable gain combination, rather than a separate physical damping measurement. The width of this region indicates sensitivity to gain selection. The PI figures are read in the same way, with KI axes varying the integral gain and the unplotted gains held at the stated optimum.

Across sea-states, we see that the starboard and port surfaces are nearly identical. The optimal bow proportional gain appears to be consistently approximately 500 N-m/(m/s), with starboard and port proportional gains of approximately 1000 N-m/(m/s) showing a similarly low variation with sea-state. Performance is much more sensitive to the integral gain selection. However, integral gains for these sea-states are generally small: this explains why there are minimal power gains moving from optimal-damping to PI control, and suggests that this conclusion may not apply to all potential sea-states.

### 7.3.2 Linear model

The linear model employs the identified PTO system rather than the full PTO model and a reduced friction model. As such, it is not entirely linear. It represents a middle-ground in

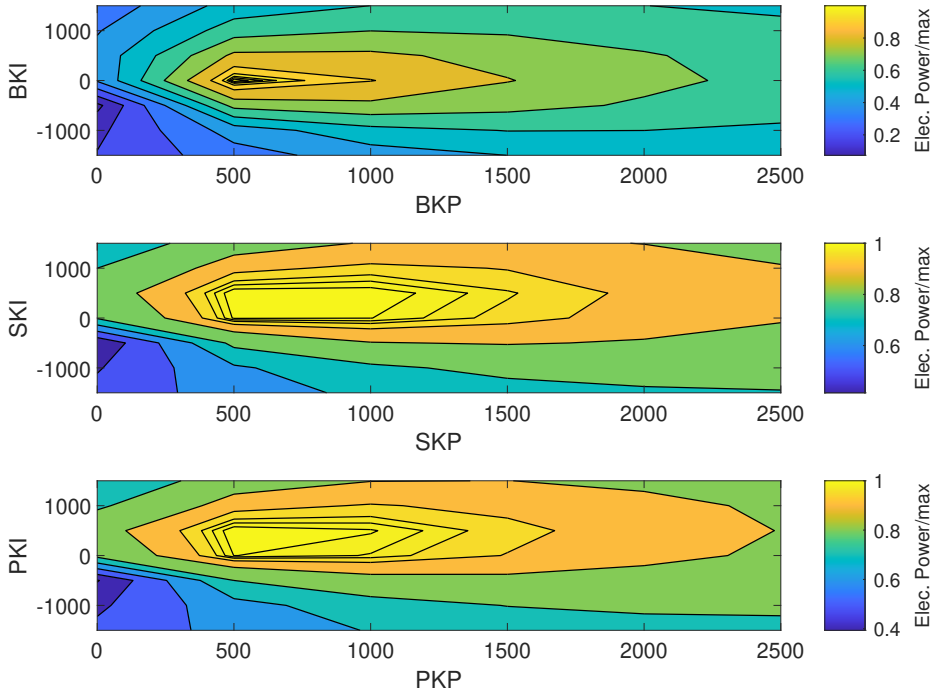



Figure 18: Frequency-domain estimated electrical power for diagonal PI control for sea-state 1.

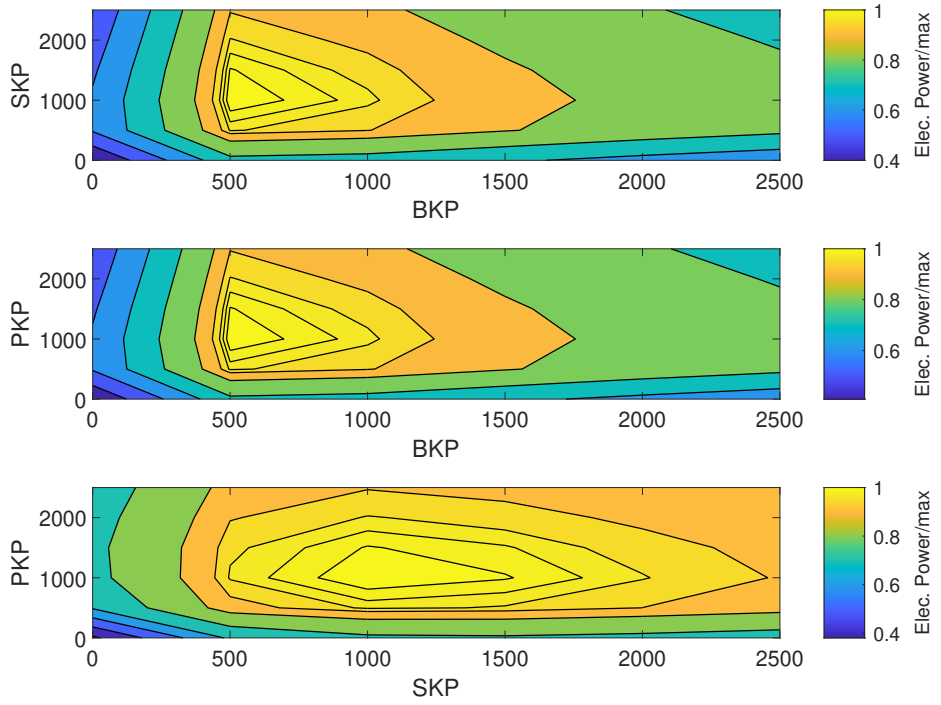



Figure 19: Frequency-domain estimated electrical power for diagonal proportional control for sea-state 2.

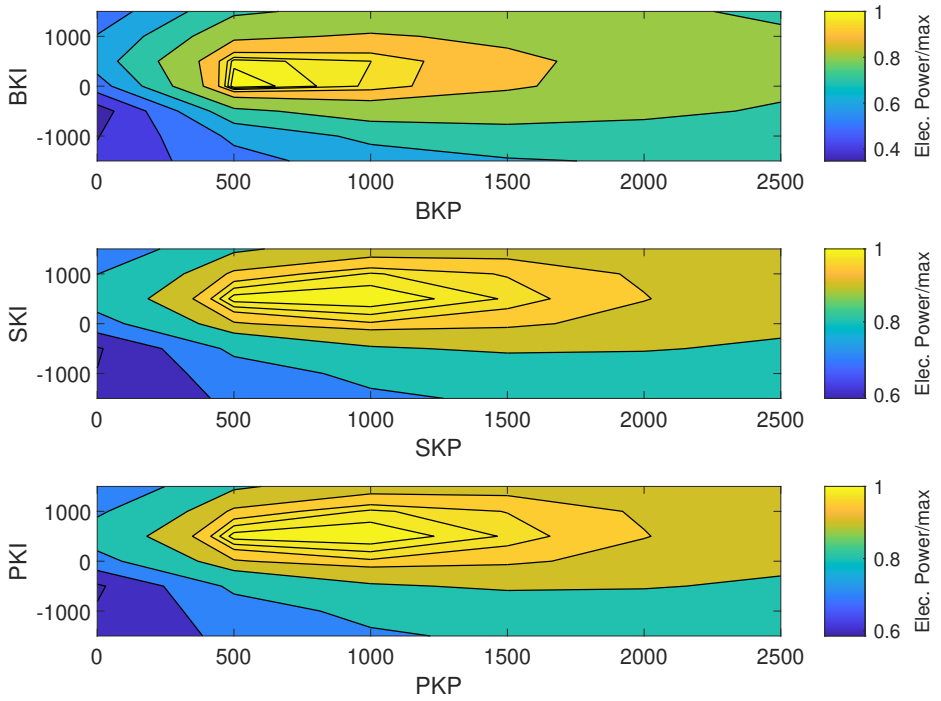



Figure 20: Frequency-domain estimated electrical power for diagonal PI control for sea-state 2.

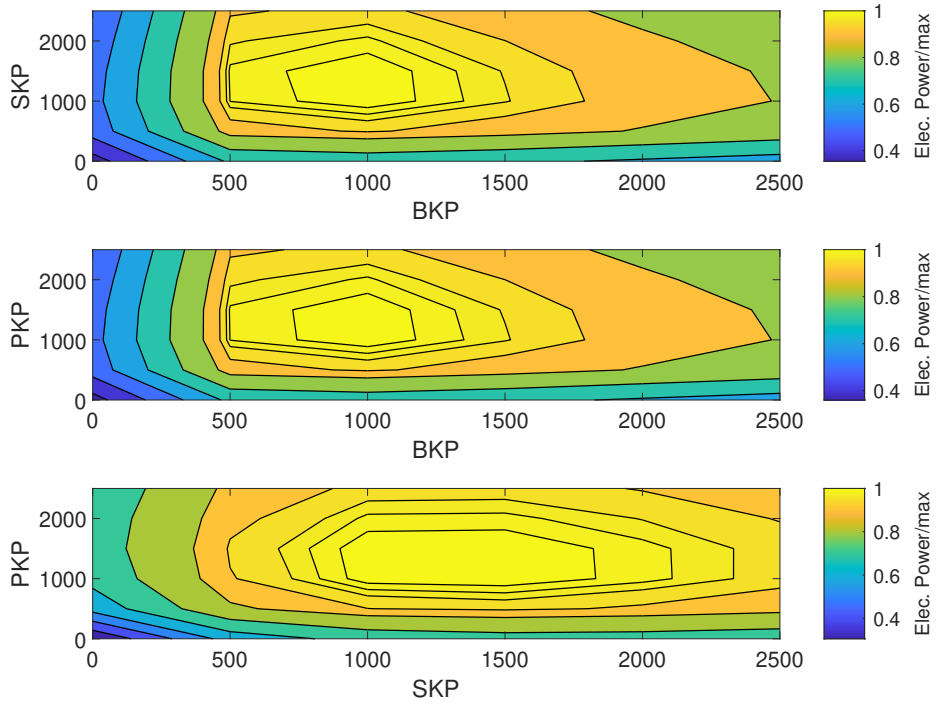



Figure 21: Frequency-domain estimated electrical power for diagonal proportional control for sea-state 3.

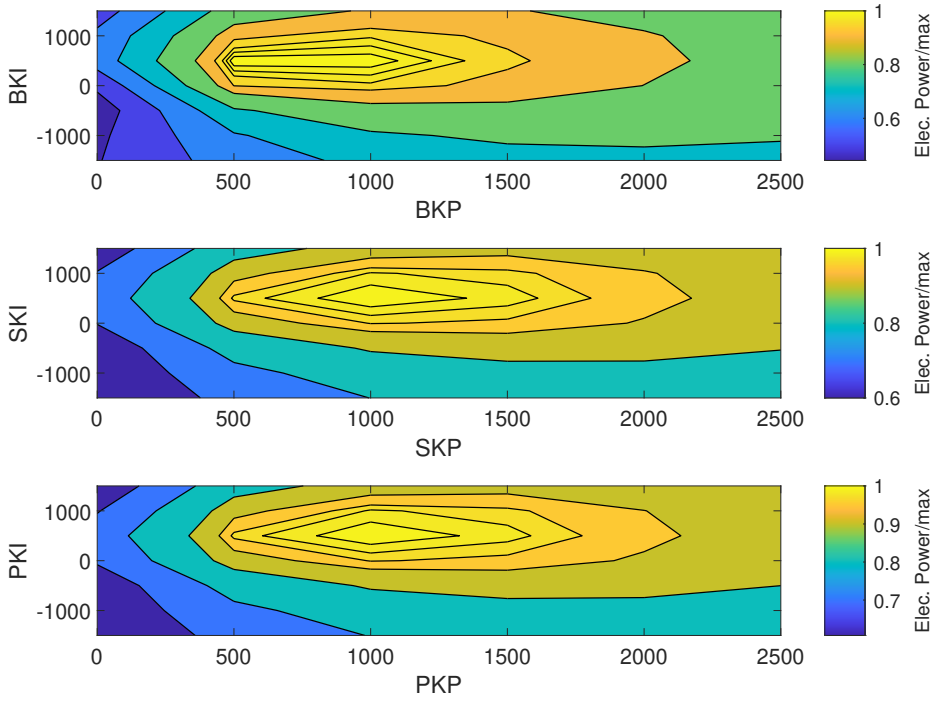



Figure 22: Frequency-domain estimated electrical power for diagonal PI control for sea-state 3.

Table 7: Linear model relative electrical power capture, with diagonal PI as a basis

| **Controller** | **SS1** | **SS2** | **SS3** |
|---|---|---|---|
| P, diagonal | 100% | 100% | 93% |
| PI, diagonal | 100% | 100% | 100% |
| P, CC | 77% | - | - |

terms of simulation speed and accuracy. It includes only linearization of the saturation limits and other discontinuities in the full PTO model and a reduced friction model. However, it utilizes the full $G$ model, using both velocity and torque inputs to prescribe tether tension, found to be significantly more accurate than the method employed by the frequency domain model.

The results for diagonal PI control are shown in Figures 23 through 25. Noting the commonalities in the starboard and port components of $Y$ and $G$, and the frequency domain results, the controller investigation space is further simplified by letting $C_{(2,2)} = C_{(3,3)}$, and thus axis with a 'SP' prefix indicate the (equivalent) starboard and port gains. A symmetric cross-coupled is attempted for this model as well: the cross coupled terms are indicated with a CC suffix, with the first two entries indicating the coupled degrees of freedom (B,S, or P). Because this controller is symmetric, the order of the prefix (i.e., SP vs. PS) is arbitrary as both terms are equal.

Unlike the frequency-domain model, there is more significant variation in optimal damping location with sea-states, though the power surface is comparatively flat in this direction versus the integral gain, to which performance is significantly more sensitive. Also notable here is that the simulation predicts instability (indicated by the white regions on the surfaces) with an overly large negative integral gain acting as a "negative spring": the surface is saturated

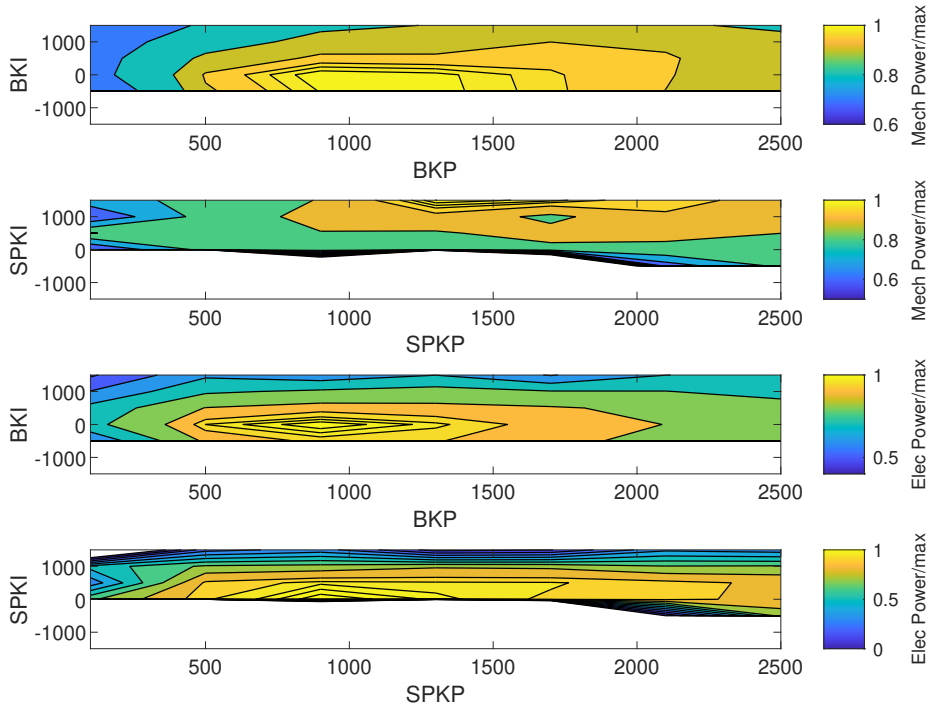



Figure 23: Linear-model estimated mechanical (upper 2) and electrical (lower 2) power for diagonal PI controller for sea-state 1.

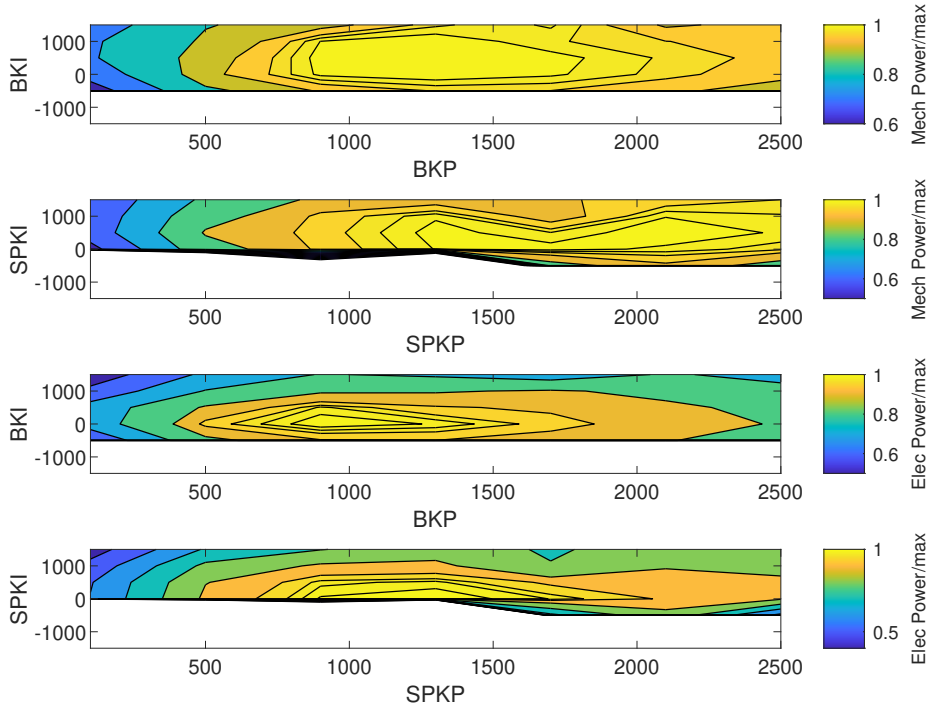



Figure 24: Linear-model estimated mechanical (upper 2) and electrical (lower 2) power for diagonal PI controller for sea-state 2.

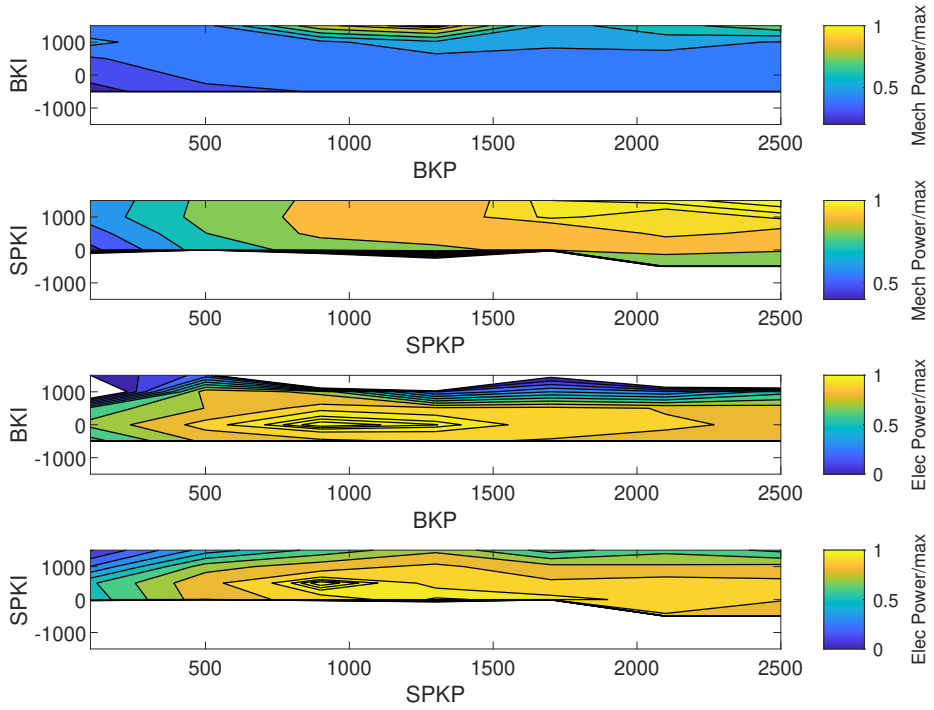



Figure 25: Linear-model estimated mechanical (upper 2) and electrical (lower 2) power for diagonal PI controller for sea-state 3.

at zero to preserve visualization near the power optimum, but in fact indicates substantial power loss at conditions approaching this instability. This aligns with physical intuition. Mechanical power optima are also presented. As anticipated, these occur at higher gains than the electrical power optima, but not significantly higher. This suggests that, as modeled, the electrical losses are comparatively minor compared to other losses present in the system.

Similar to frequency-domain predictions, the optimal integral gains are relatively small and as such, there is minimal additional power capture resulting from their inclusion in the evaluated sea-states. In fact, in all but sea-state 3, the optimal attempted integral gain is zero. It is possible that a finer discretization of attempted integral control gains may show more substantial benefit, but it is nonetheless predicted to be slight overall.

Observing the increased performance of controllers including off-diagonal terms, a symmetric (i.e., $K_P(m,n) = K_P(n,m)$) cross-coupled proportional controller was also investigated for the linear model. Similar to PI control, the diagonal terms $K_P(2,2) = K_P(3,3)$ given the similarity of the starboard and port impedance functions and the near-equivalence of these optimal gains identified in the frequency-domain models. Of the controllers tested, these offer the highest energy capture, although the extent of the improvement over diagonal controllers are a strong function of sea-state.

These power surfaces for cross-coupled gains are much more featured than the diagonal controllers (Figure 26 and 27). Particularly, they are frequently non-convex and fairly flat over large gain windows: this may pose difficulty for any optimization approach. Further, the location of the optimal cross-coupling gains vary strongly by sea-state, frequently changing sign. As noted, proper selection of these gains can increase power capture by a moderate amount, but improper selection can severely limit power capture or cause instability (unstable simulated cases are indicated by white on the contour surfaces).

Only the results from the first sea-state are presented here and included in the table.

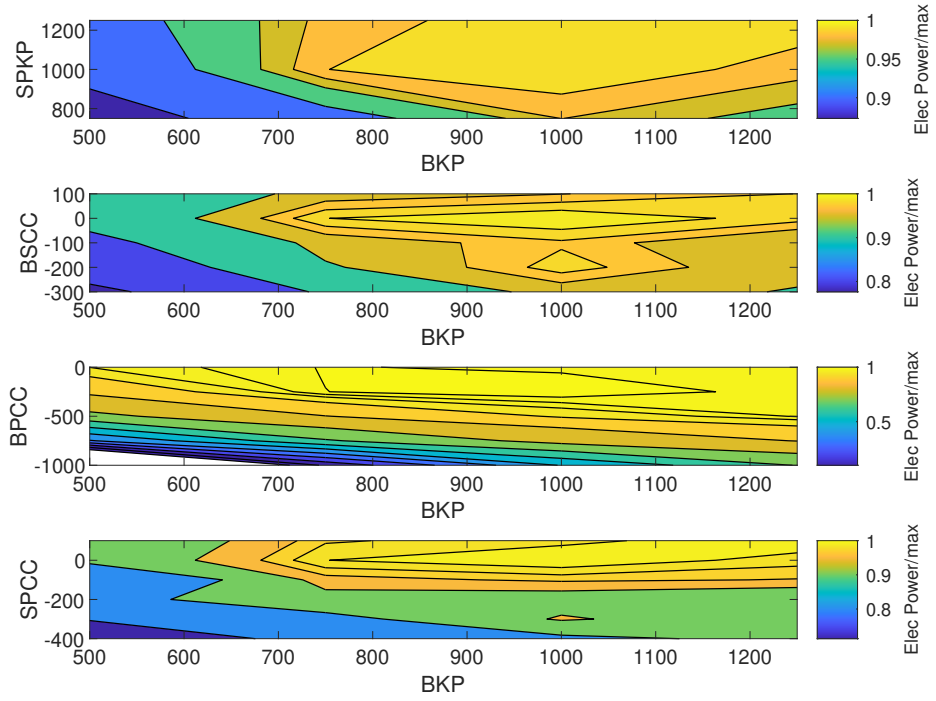



Figure 26: Linear-model estimated electrical power for the simplified cross-coupled P controller for sea-state 1, as a function of bow gains.

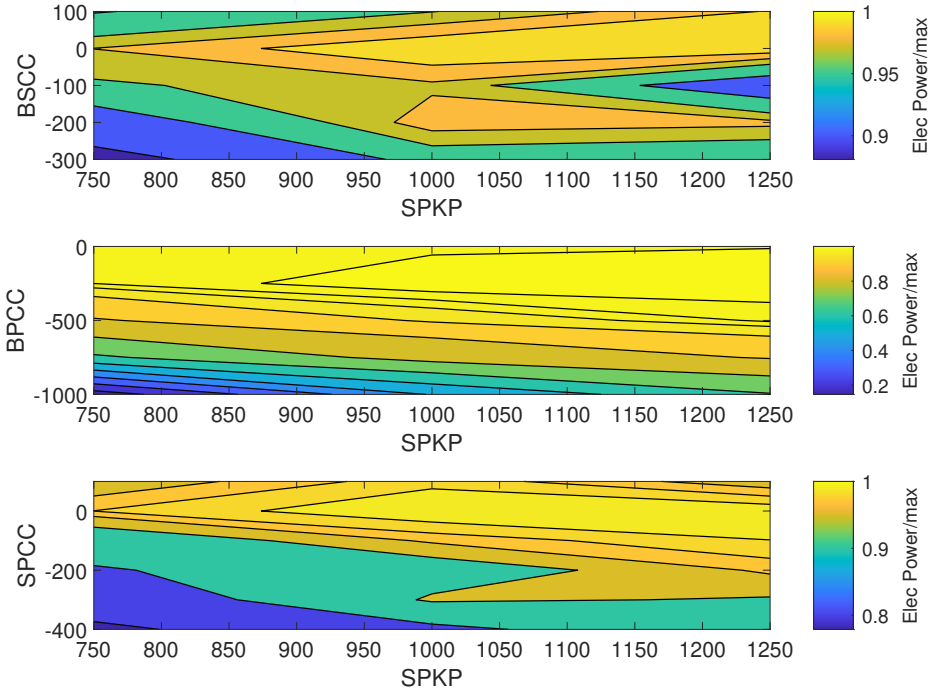



Figure 27: Linear-model estimated electrical power for the simplified cross-coupled P controller for sea-state 1, as a function of starboard and port gains.

Table 8: Full model relative electrical power capture, with diagonal PI as a basis

| **Controller** | **SS1** | **SS2** | **SS3** |
|---|---|---|---|
| P, diagonal | 100% | 100% | 100% |
| PI, diagonal | 100% | 100% | 100% |
| PCC | 94.4% | 102% | 102% |

Results from SS2 and SS3 have strong resonance peaks that are an artifact of the utilized transfer functions that severely over-estimate power capture and do not provide useful predictions. Additionally, comparing the presented predictions for sea-state 1 to the analogous controller results on the full model indicates that for the cross-coupled controller, the linear models are not useful predictions of full model performance.

### 7.3.3 Full model

The full model is identical to the linear model except that it uses the detailed PTO model and the full static friction model. In this way, it is anticipated to be the most accurate of the presented methodologies. Additionally, this is the only model for which the time-responses of PTO components are available (e.g., accumulator fluid levels), which are likely of design significance. However, this model takes significantly longer to run, is the most difficult to debug, and is of sufficient complexity that Simscape solvers can struggle to converge. With this in mind, the modifications presented in Section 7.2 were performed to improve model performance while preserving accuracy.

An additional modification was made during the closed-loop controller study. In lieu of the simplified electrical model, an ideal torque source in series with a low-pass filter (to match time constant) and a saturation block (to affect torque limit) was used to apply the prescribed generator control torque. This was to avoid an error that arose intermittently related to the electrical side of the simplified model, which was simply an ideal DC voltage source. The effect of drive losses are applied to the energy calculation in post-processing based on the torque and speed values and Figure 5. For values off of this table, an efficiency of 0.85 was assumed: while this value has a minor effect on the total power estimates, this value does not significantly impact the shape of these power surfaces. In the case of the power limit, the simplified drive applies this limitation to the product of the drive efficiency and the instantaneous mechanical power, when in fact this 35 KW limit is a grid-side export limitation. Given that there are additional dump resistors available this power limit is unlikely to ever affect the allowable generator torque application itself.

A full system model with the simplified electrical drive implementation is also included, but was poorly suited for the large control batch runs due to the aforementioned errors.

The full-model power surfaces are similar to that of the linear model, suggesting that, as an estimate of power, the much-faster linear model can be effectively utilized in lieu of the full model. The full model does indicate that power capture does not reduce as steeply for larger proportional gains. This may be an effect of a non-linearity, such as a saturation limit. To investigate this, the portion of time a torque command exceeded the saturation limit (3300 N-m) is plotted as Figures 34 through 36.

Inspection of the saturation surfaces indicate that at larger gain values (particularly those approaching instability due to an overly large negative spring effect), the torque command is more regularly saturated (Figures 34 through 36). This is a likely explanation for the decreased sensitivity of the power surface to elevated proportional gains, and suggests that in other sea-states for which optimal proportional gains may be elevated, the present torque

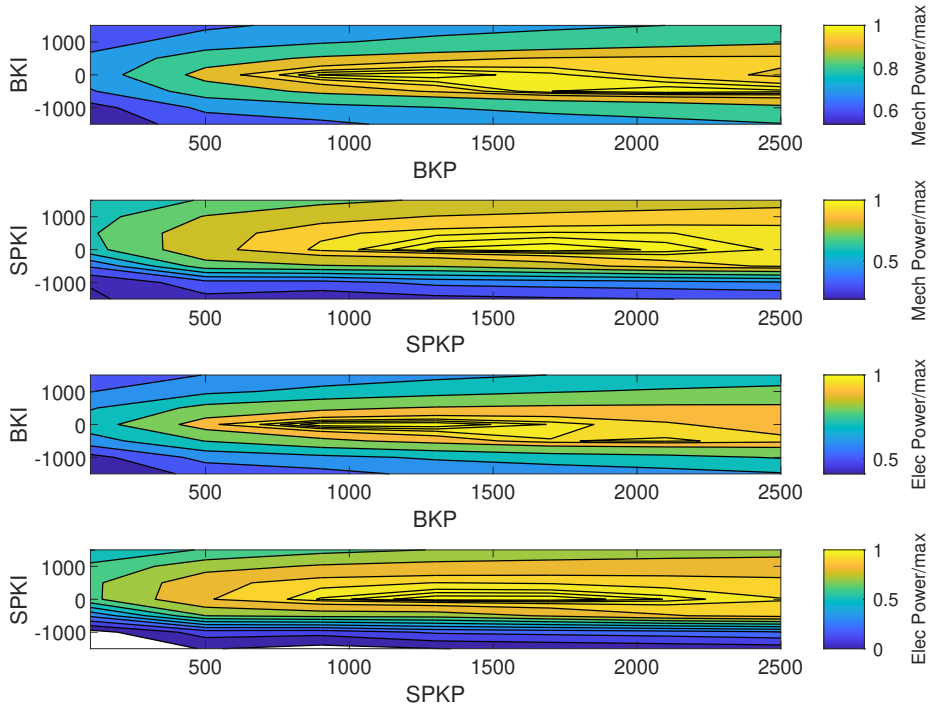



Figure 28: Full model estimated mechanical power (upper 2) electrical power (lower 2) for diagonal PI control for sea-state 1.

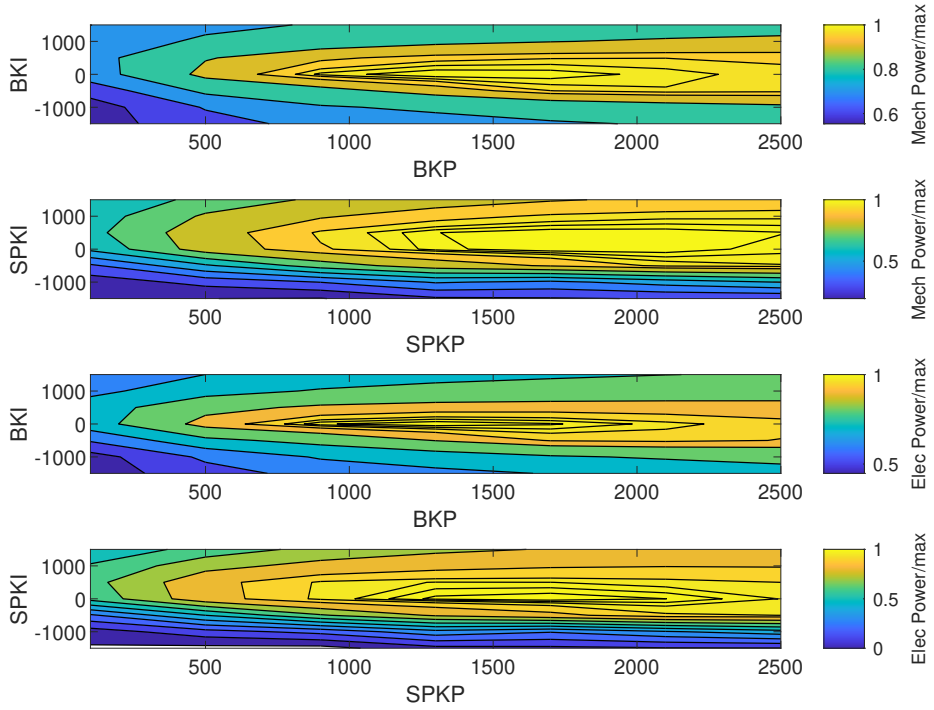



Figure 29: Full model estimated mechanical power (upper 2) electrical power (lower 2) for diagonal PI control for sea-state 2.

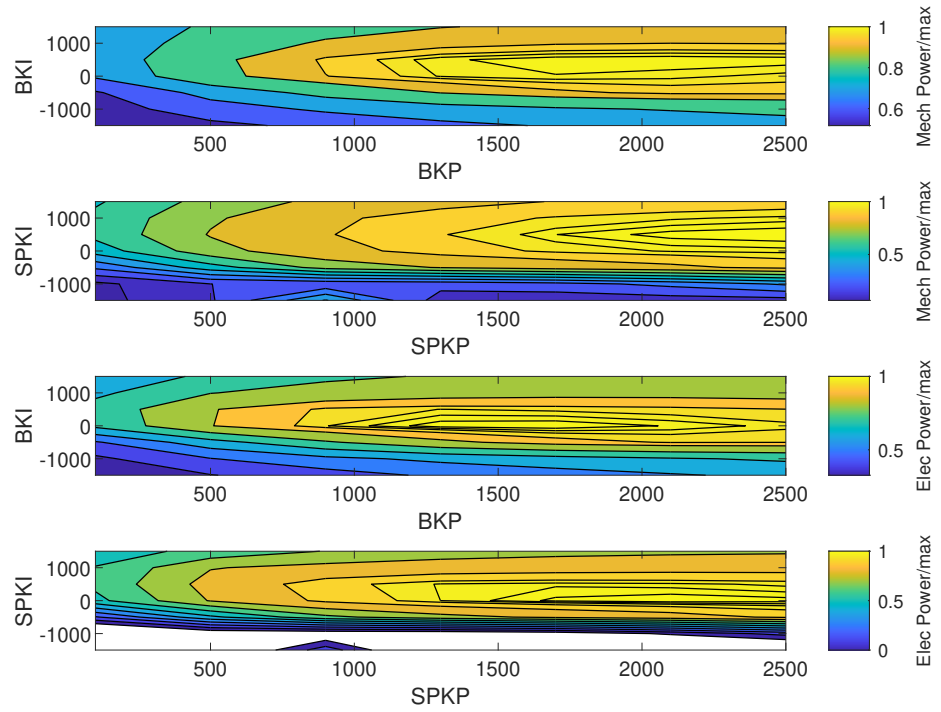



Figure 30: Full model estimated mechanical power (upper 2) electrical power (lower 2) for diagonal PI control for sea-state 3.

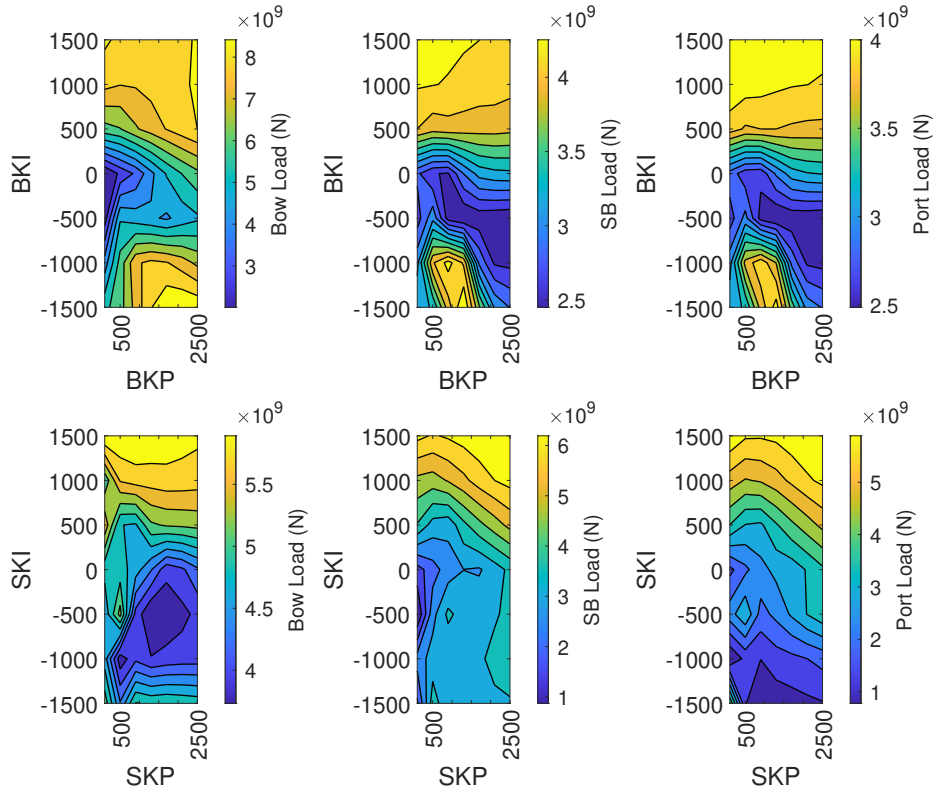



Figure 31: Full model estimated cable load variance for sea-state 1.

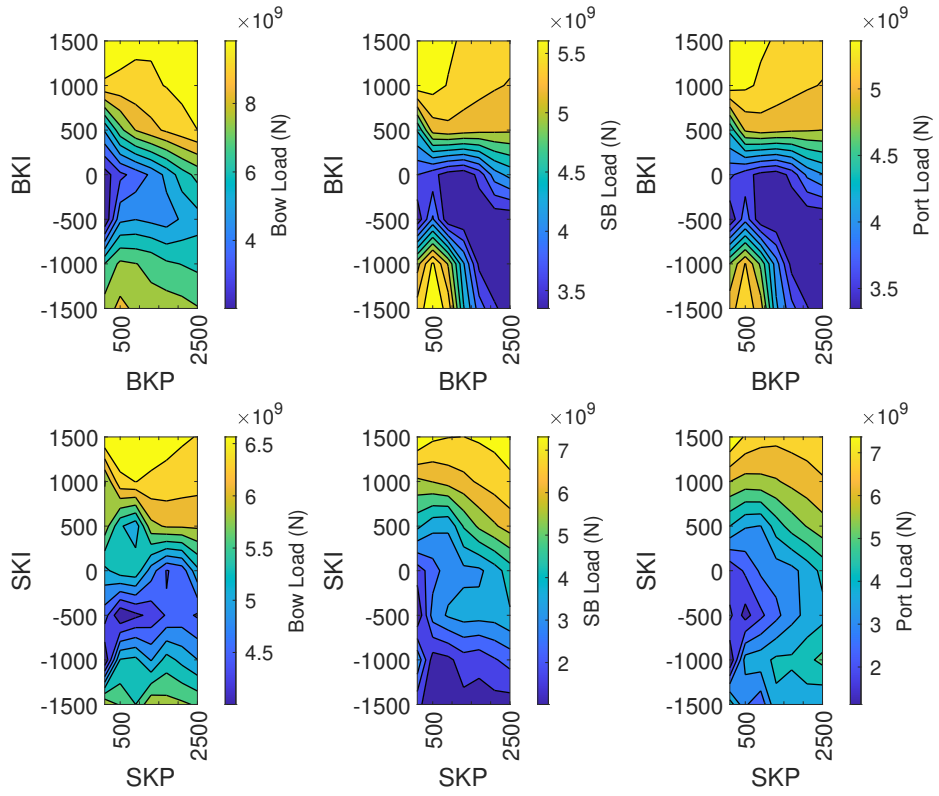



Figure 32: Full model estimated cable load variance for sea-state 2.

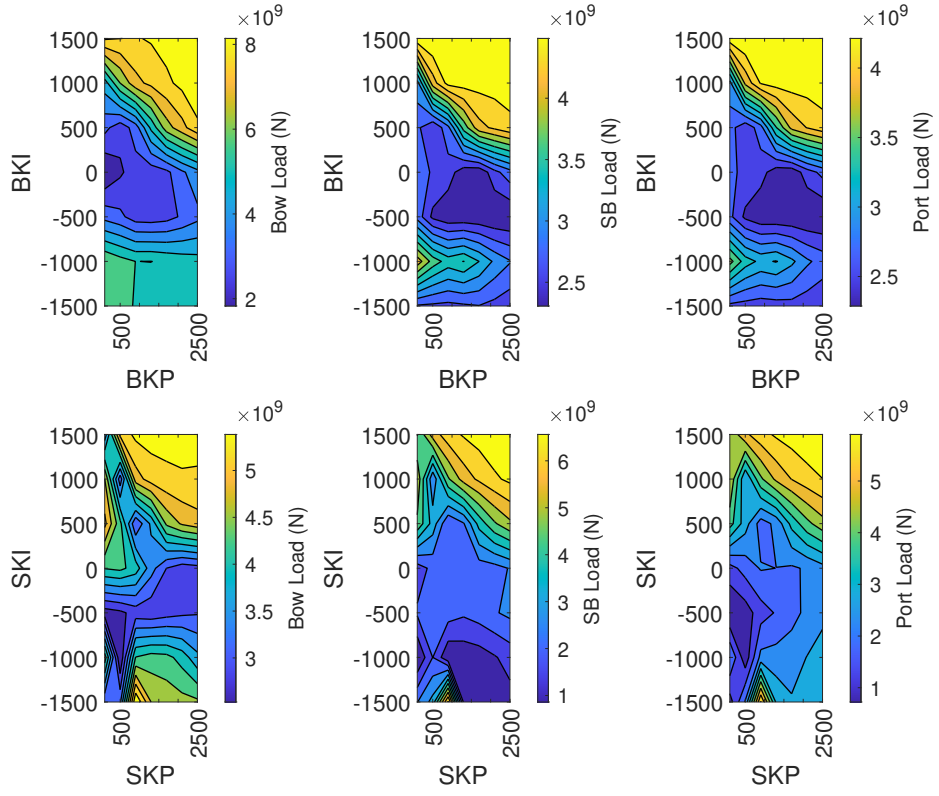



Figure 33: Full model estimated cable load variance for sea-state 3.

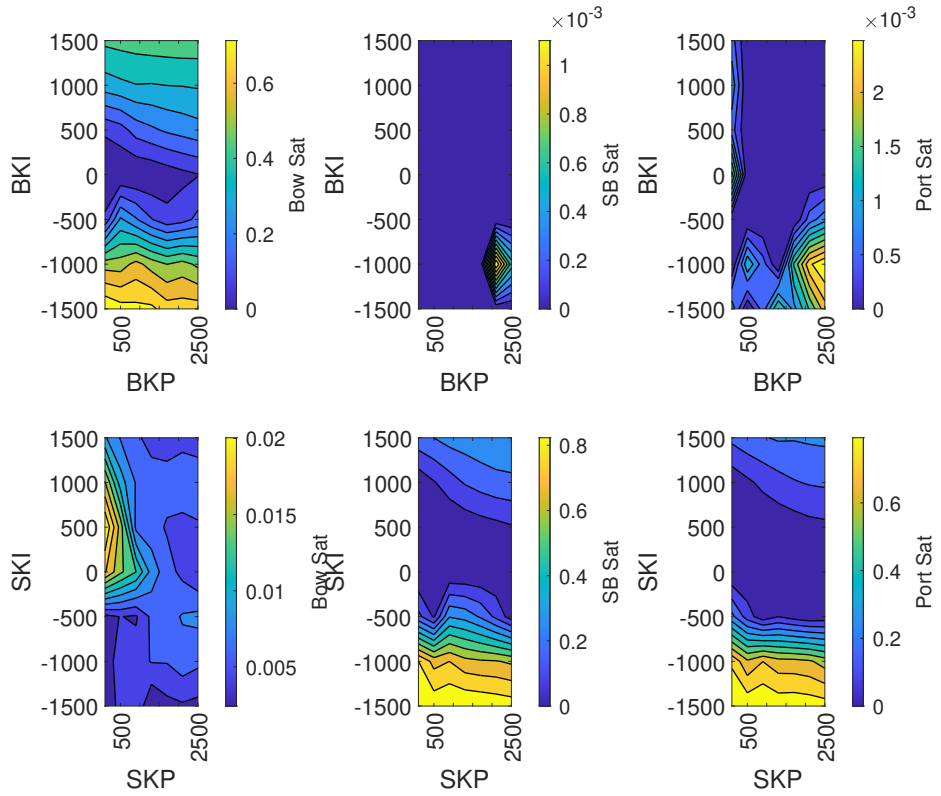



Figure 34: Full model estimated drive saturation portion for sea-state 1.

rating of the motor may be inadequate to affect optimal control.

The variance of tether tension is a quantity of interest for the fatigue life of the tethers. Surfaces of tether tension variance as functions of controller gains are presented as Figures 31 through 33. Notably, the maxima of tether tension variance are not co-located with electrical power-optimal gains, however tether tension variance can be reduced if necessary by selecting gain combinations that are sub-optimal with regard to electrical power.

Because of the performance increases suggested by the frequency domain and linear models, a simplified symmetric cross-coupled proportional controller (i.e., $K_P(m,n) = K_P(n,m)$), $K_P(2,2) = K_P(3,3)$) was also examined on the full model. Compared to the linear model result presented, the performance effects and the surfaces are less striking. The power surfaces appear convex, though flat. Notably, the optima appear to be at one extreme high-gain of the investigated space. Though plots from single cases are presented, several runs with higher gain ranges were also attempted, and this was a robust result, although the power surface becomes very flat above a certain value. This is because (as indicated in plots of the saturation portion Figures 46 through 47) the controller begins saturating against the torque limit such that increases in gain do not result in significant increases in power.

Of particular interest is sea-state 1, which actually indicates a reduction in total power capture with the cross-coupled terms. This is not real: in order to maintain tractable batch run numbers in the now 5-dimensional controls space, the discretization of each dimension of that space is reduced. As such, the tested proportional control gains did not contain the previously observed optimal proportional result. Instead, this indicates that the optimal cross-coupled gains for this case are zero in all cases, and the optimal proportional controller is diagonal in form.

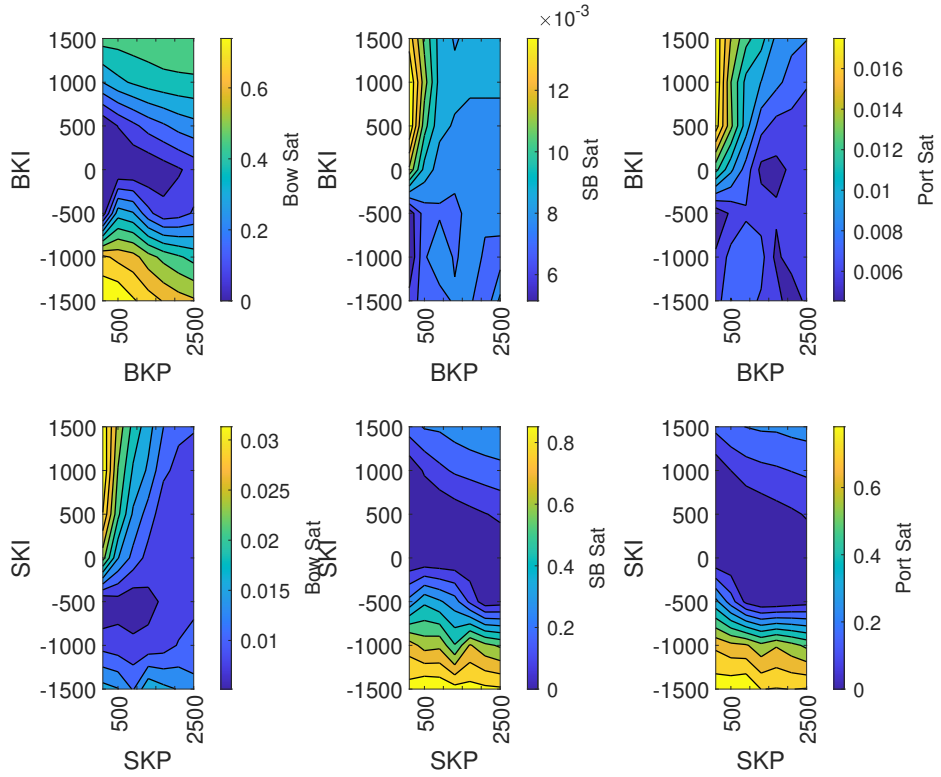



Figure 35: Full model estimated drive saturation portion for sea-state 2.

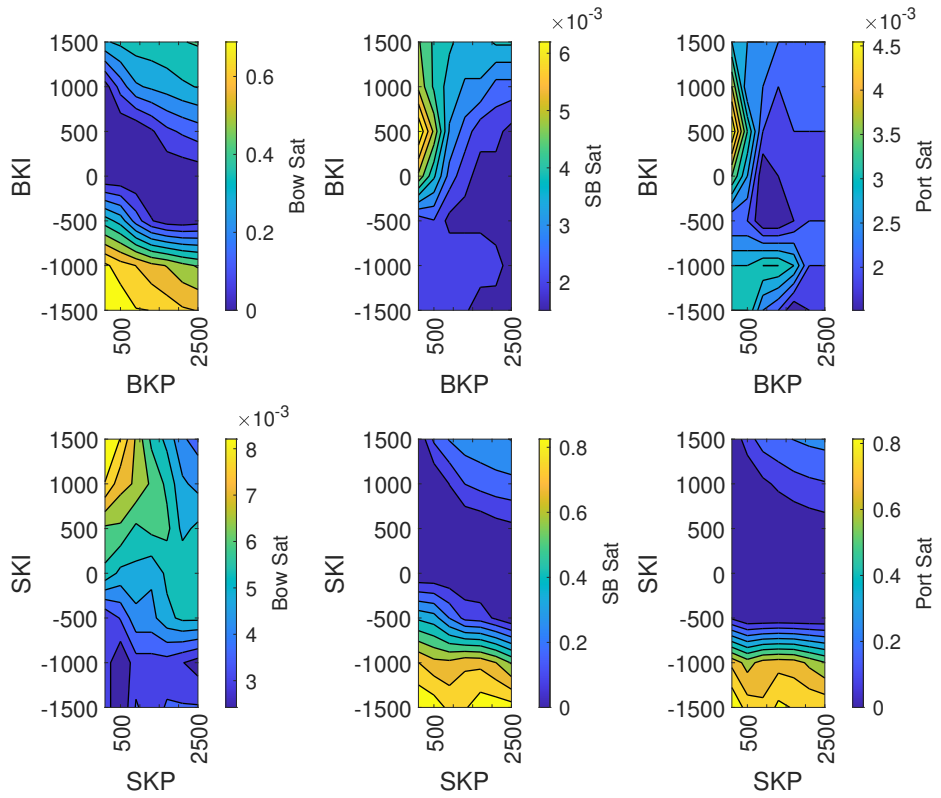



Figure 36: Full model estimated drive saturation portion for sea-state 3.

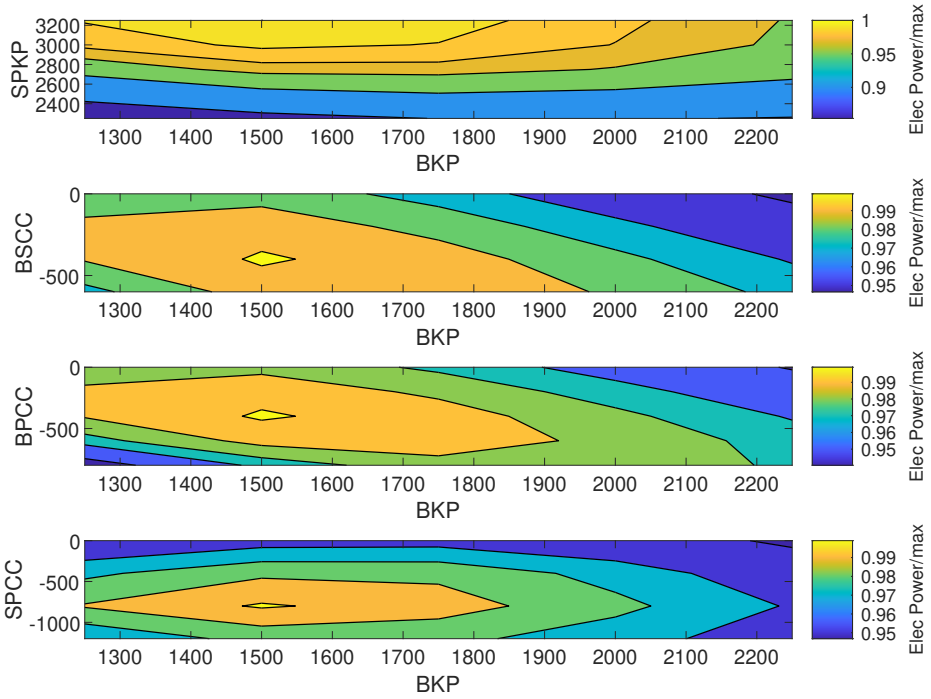



Figure 37: Full model estimated electrical power for the simplified cross-coupled controller for sea-state 1, as a function of bow gains.

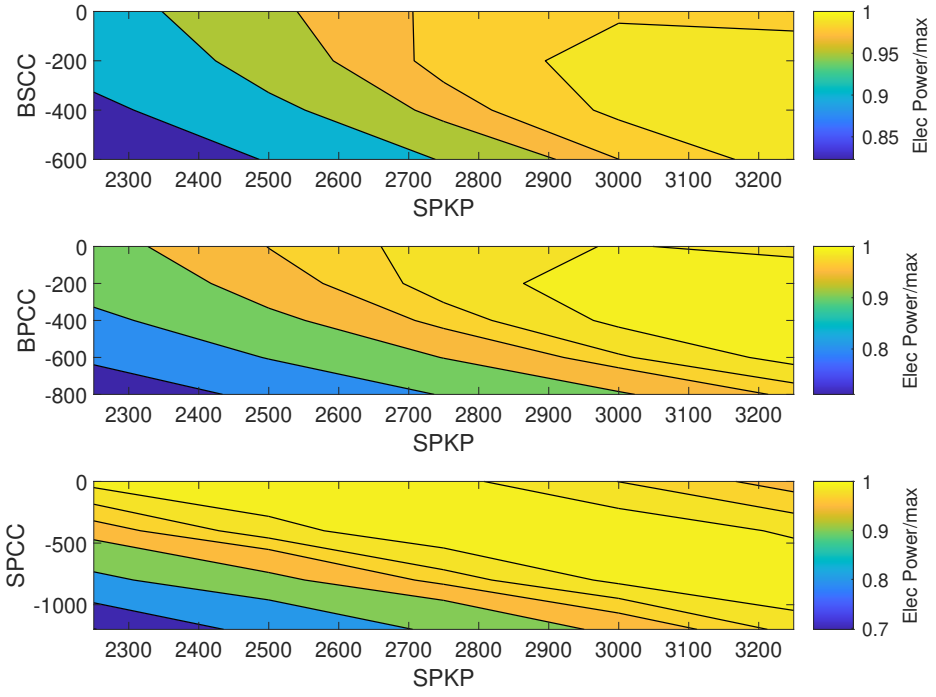



Figure 38: Full model estimated electrical power for the simplified cross-coupled controller for sea-state 1, as a function of starboard gains.

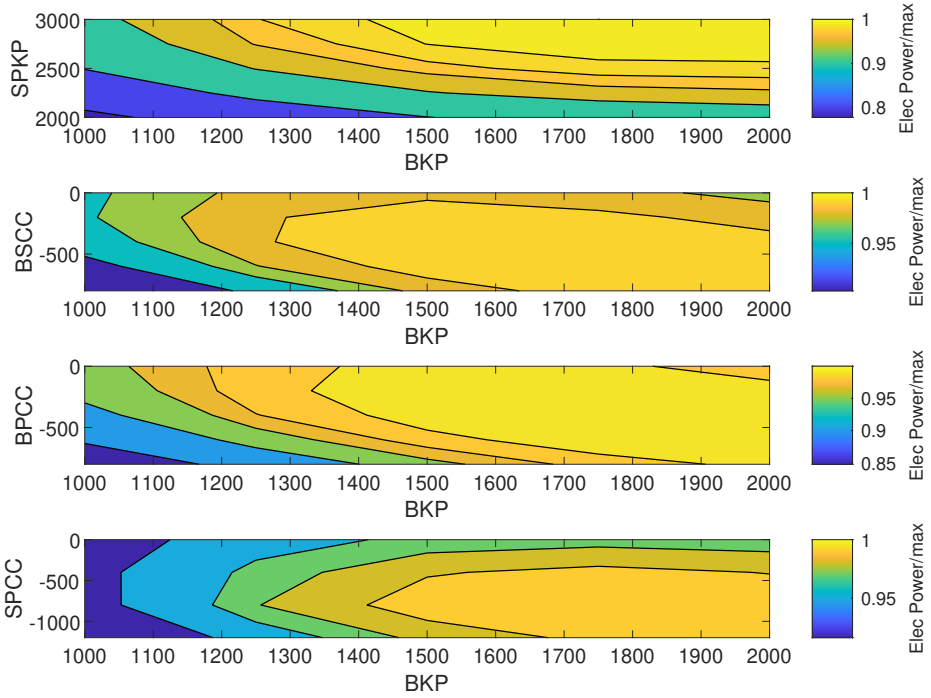



Figure 39: Full model estimated electrical power for the simplified cross-coupled controller for sea-state 2, as a function of bow gains.

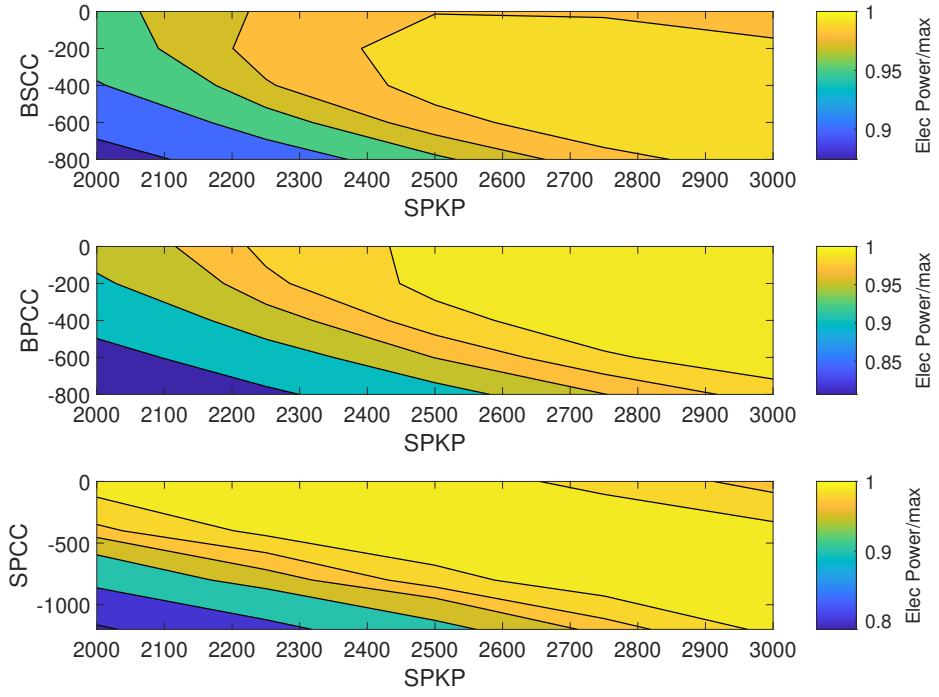



Figure 40: Full model estimated electrical power for the simplified cross-coupled controller for sea-state 2, as a function of starboard gains.

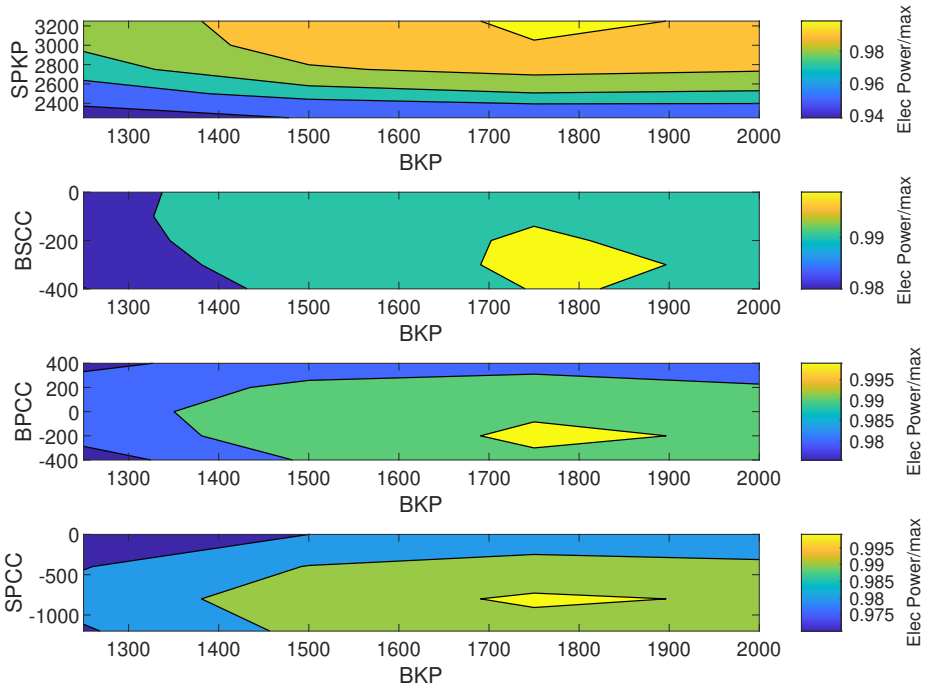



Figure 41: Full model estimated electrical power for the simplified cross-coupled controller for sea-state 3, as a function of bow gains.

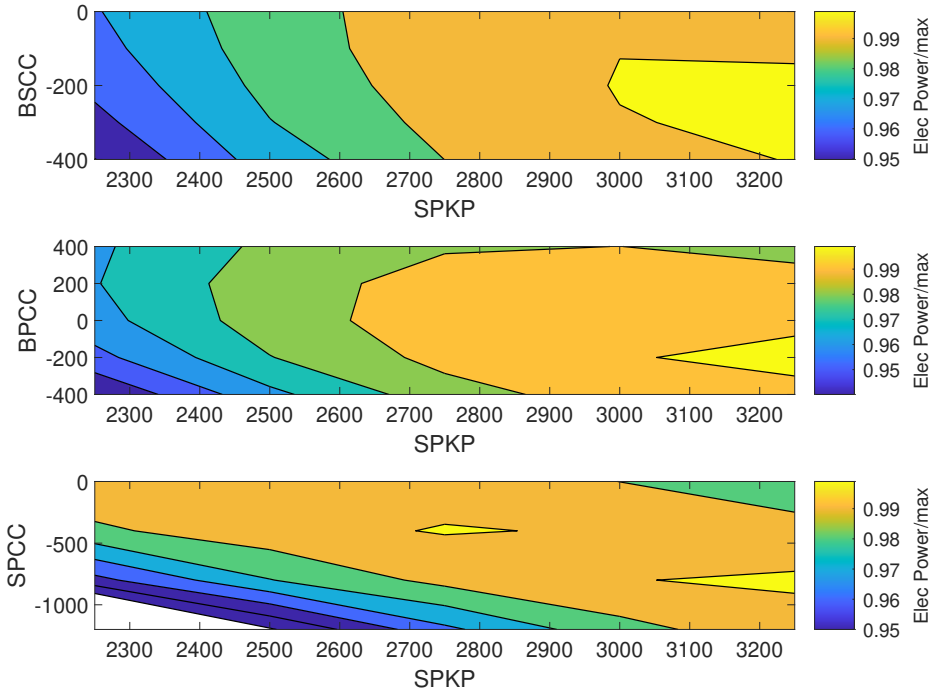



Figure 42: Full model estimated electrical power for the simplified cross-coupled controller for sea-state 3, as a function of starboard and port gains.

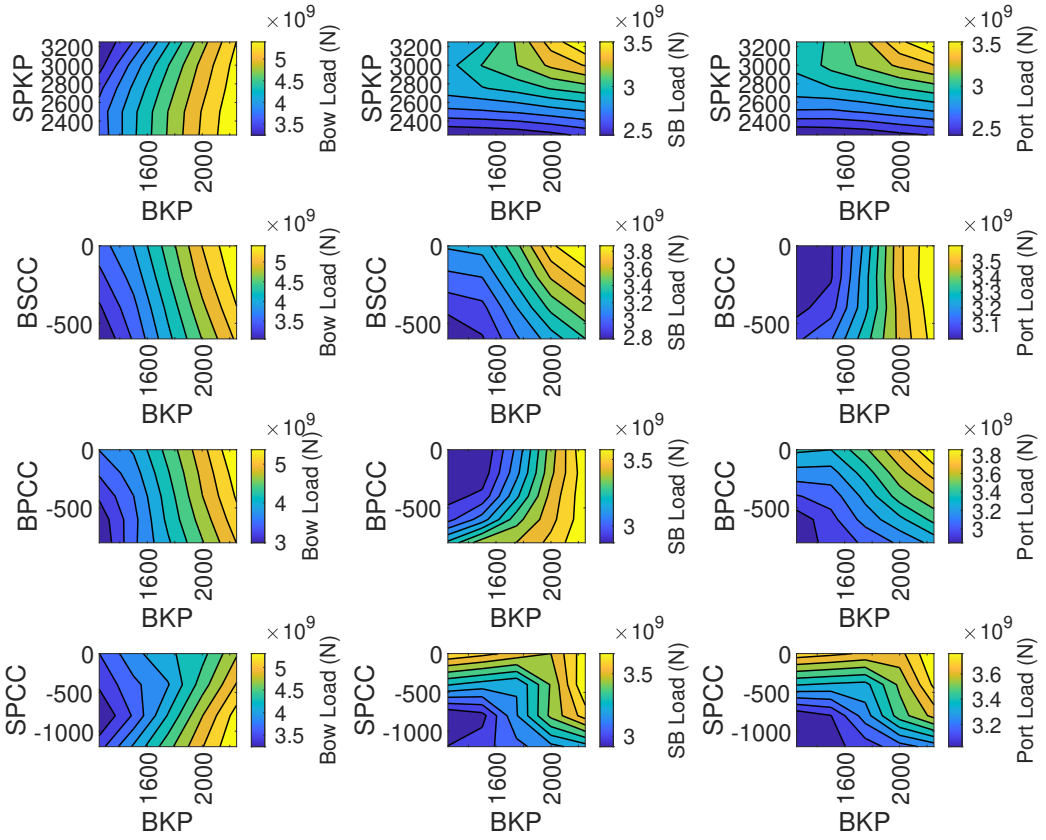



Figure 43: Full model estimated cable load variance for the simplified cross-coupled controller for sea-state 1.

The maximum cable load variances again do not tend to occur near optimal gain combinations, with the diagonal gains (i.e., $K_P(1,1)$, $K_P(2,2)$) having a stronger influence on their respective DOF than any associated cross-coupling term, though there are exceptions. Notably, the bow-port cross-coupling gain shows a more significant effect on port cable loads than the port proportional gain in sea-state 2. Predictably, the weakest effect tends to be gains associated with other degrees of freedom (i.e., bow and bow-port cross couplings' effect on starboard cable load), though this is non-zero and should not be neglected, particularly if cable fatigue is a paramount concern.

Finally, as noted in the previous section, the predicted controller optima and performance differ markedly between the linear models and the full system model for the cross-coupled controllers. It is not recommended that these simplified system models are used for controller design.

### 7.3.4 Post-hoc modifications for increased stability

The simulation will error out if the state of any component is outside of physical bounds: for instance, an accumulator pressure of less than absolute zero. While the physical system will not actually reach this state, a failed model run is nonetheless indicative of an undesirable operating condition. The following modifications were made to the model to run consistently to nearly optimal proportional gains.

1. Low pressure, recharge, and auxiliary accumulator volume increased

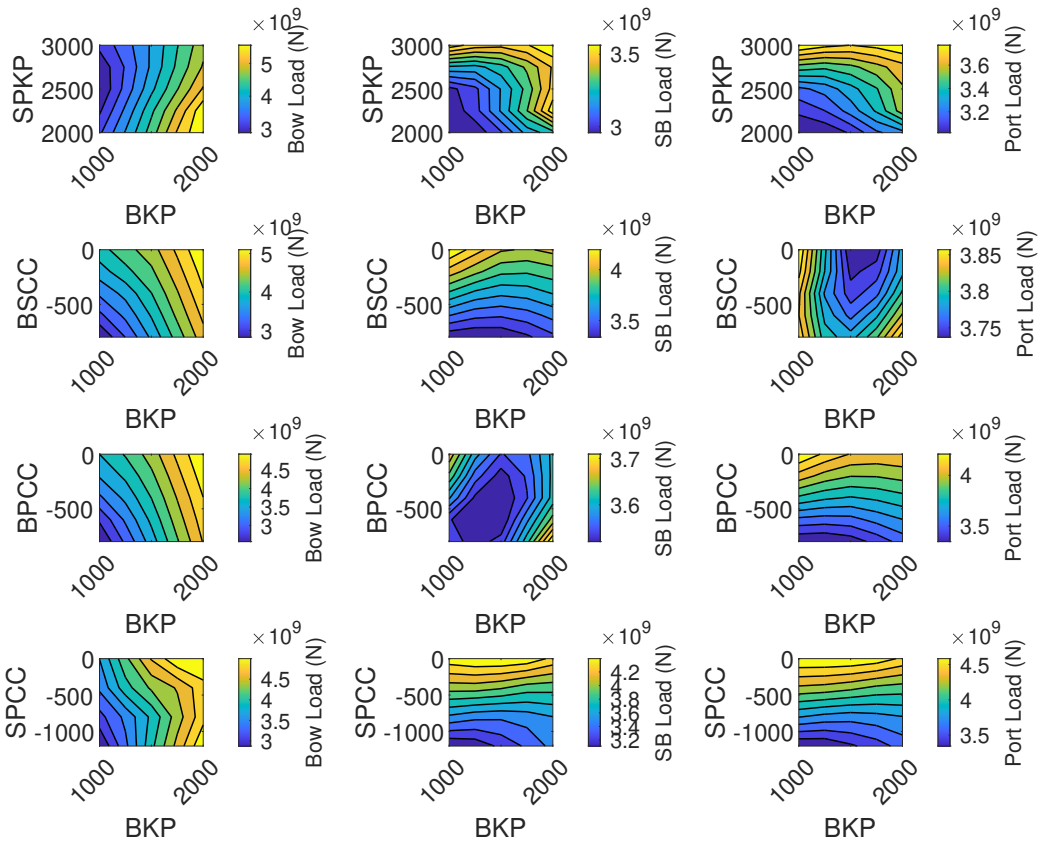



Figure 44: Full model estimated cable load variance for the simplified cross-coupled controller for sea-state 1.

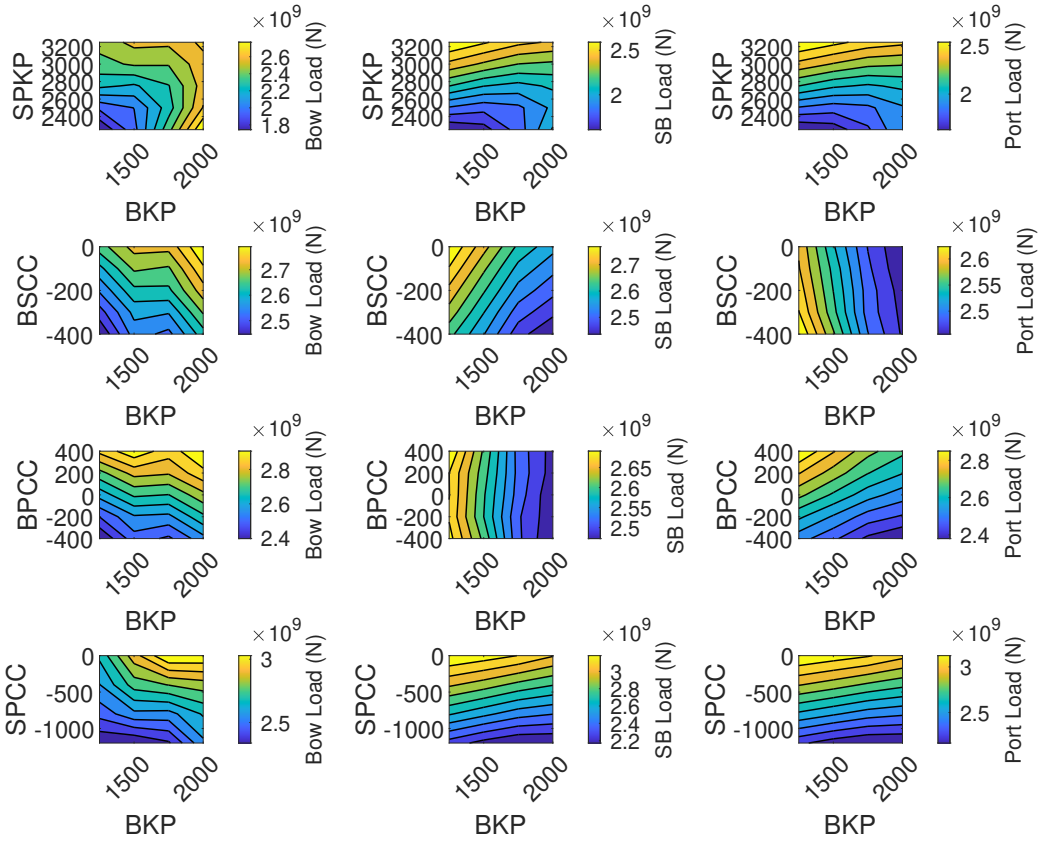



Figure 45: Full model estimated cable load variance for the simplified cross-coupled controller for sea-state 2.

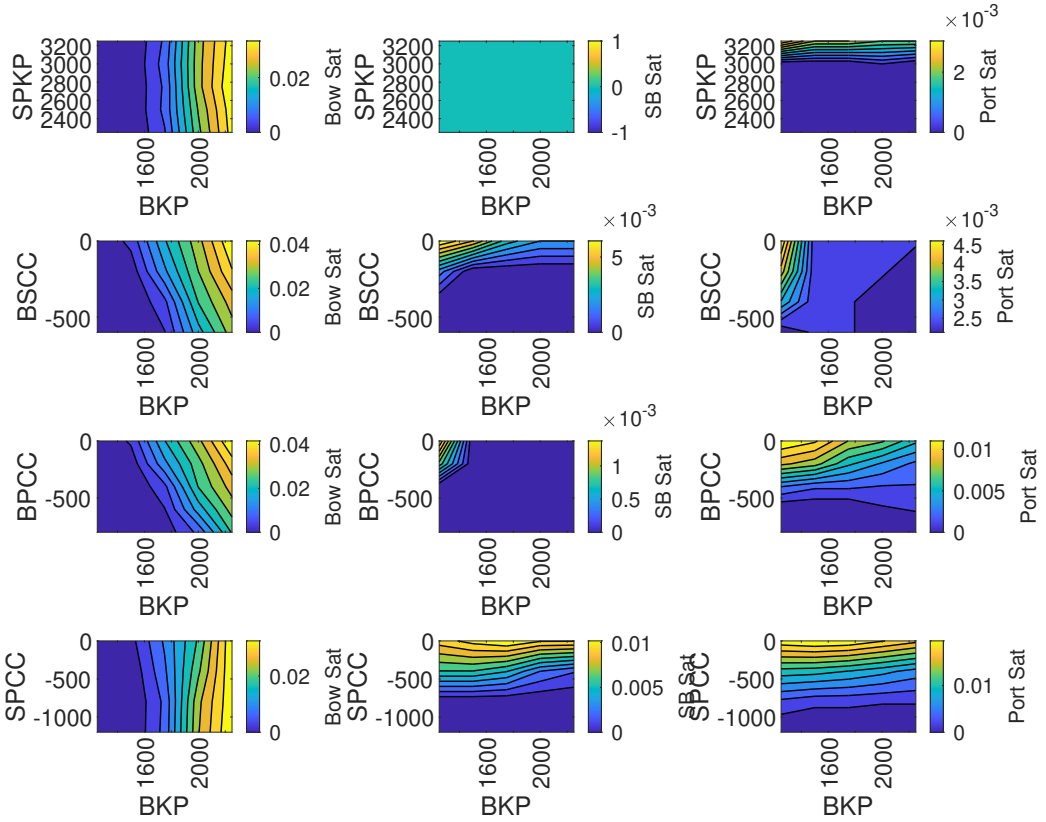



Figure 46: Full model estimated saturation portion for the simplified cross-coupled controller for sea-state 1.

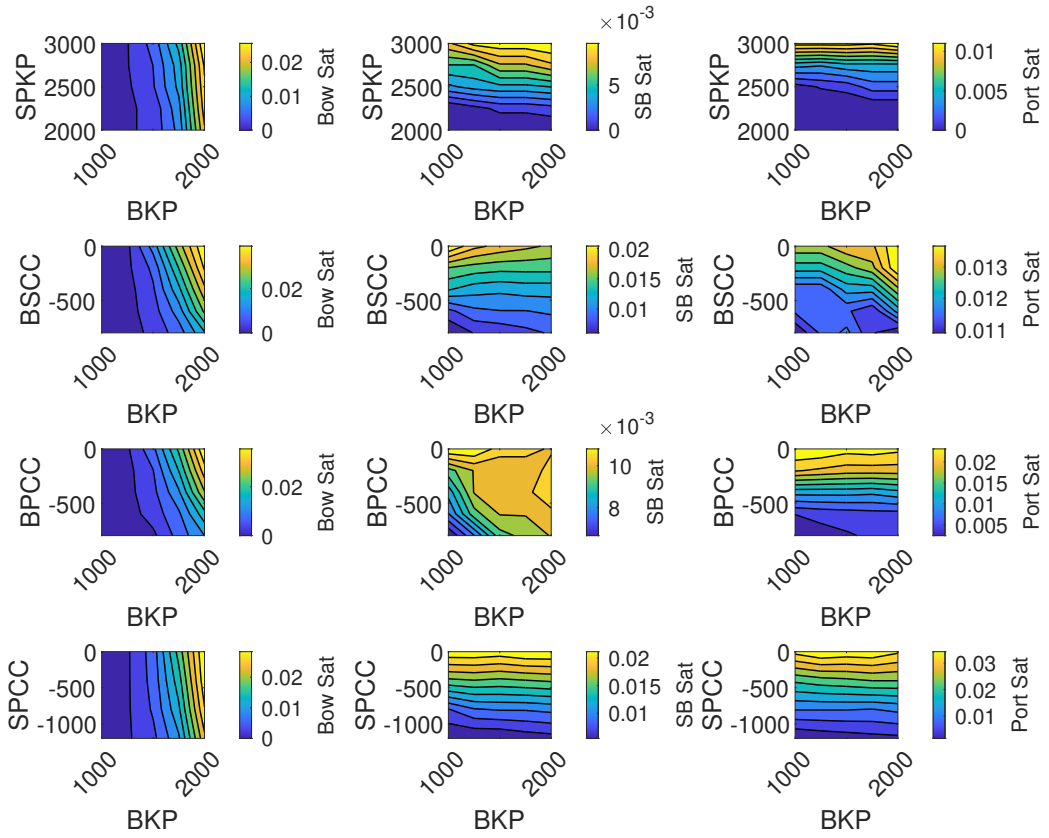



Figure 47: Full model estimated saturation portion for the simplified cross-coupled controller for sea-state 2.

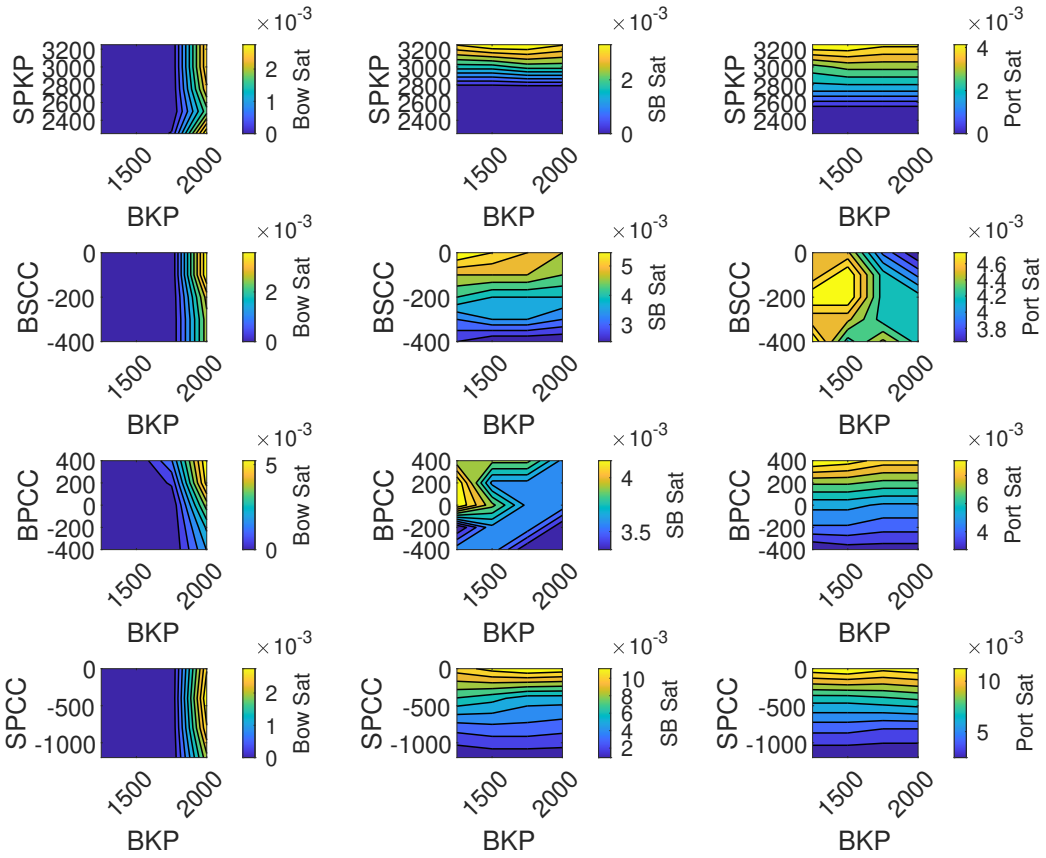



Figure 48: Full model estimated saturation portion for the simplified cross-coupled controller for sea-state 3.

2. High-pressure accumulator gas volume decreased to smallest prescribed condition (i.e., effective stiffness increased)

3. Shaft inertias removed.

It is also recommended that the recharge logic is reconsidered: as it stands, a "positive" displacement of the tether for a sufficiently long time open a valve causing the high-pressure accumulator to be refilled. However, a positive displacement of the tether will yield a positive pump displacement which will, assuming there are no over-pressure conditions, already have pushed more fluid into the high-pressure accumulator. The result can look like positive feedback. This counter-intuitive approach was discussed with OPI and it was concluded that this was the desired behavior. However it is suggested that this implementation is reviewed by OPI. In particular, it may be more prudent to inform this recharge logic based upon high-pressure accumulator piston position, rather than tether position, to prevent the high-pressure accumulator from fully discharging, as was observed to happen in some simulations. Notably, the recharge accumulator intended to ensure that this high-pressure accumulator does not fully discharge does not itself show large volume changes. This problem is not seen to the same extent on the starboard and port accumulators, but this likely because the excitation and impedance models are derived for a wave-heading aligned with the bow: oblique waves more directly impacting the port and starboard PTOs will likely cause a similar issue.

### 7.4 Suggested System Modifications to Enhance Performance

There appears to be significant loss of energy due to static-friction at the pumps, which is both difficult to model and, particularly in smaller sea-states, reduces efficiency. Based on simulation results alone (i.e., author has limited understanding of the actual physical or component-level design constraints of the device), simply increasing the torque, power, and speed limits of the generator does not enhance performance. In isolation, these increases often cause the simulation to fail by depleting an accumulator or otherwise drawing a vacuum in the hydraulic system, or causing another edge-case operating condition that is difficult to simulate and results in solver failure. Changes in generator sizing must be made in conjunction with modifications to the hydraulics to increase power capture.

A comparison of the mechanically-optimal and electrically-optimal gains suggest that the resistance of the electrical components does not markedly change the effective impedance of the device. This can imply that electrical losses for the as-modeled system are not as significant as other sources of damping in the system.

### 7.5 Lesson Learned and Test Plan Deviation

The timeline of this project was extended due to the difficulties developing a closed-loop model of sufficient complexity to capture all of the relevant dynamics. We were provided with an open-loop model of the system, however this model had to be heavily modified to accommodate the closed-loop controls investigation: the developed model approaches the limits of Simscapes' simulation capabilities. A close collaboration was needed with MathWorks representatives and several advanced techniques were developed in order to consistently simulate to reasonable accuracy. In future TEAMER projects it is recommended that any existing models to be built upon or modified are provided to the facility during collaboration on the application and/or budget and timeline determination. In this case, the provided model was highly complex, with limited documentation, and took significant time to understand the

dynamics of system and the specific modeling limitations that would be encountered. Functionally this may be difficult, as non-disclosure agreements are not typically in place until the beginning of a project. But it can also be difficult to anticipate, from the deliberately non-specific conversations held outside of an NDA, the technical complexity (and associated cost and time) of such an undertaking.

Specifically, decoupling hydrodynamic solvers from complex PTO models introduces the difficulty that a proxy system (in this case, a family of linear impedance models) must be introduced to the PTO model to incorporate hydrodynamics. These models typically share the form of outputting the device velocity as a function of the input total force (excitation and PTO forces) exerted on the body. In a feedback system, this implies that the input to the PTO model must then be a velocity source. This is problematic from a numerical perspective in the simulation of any discontinuous elements, particularly static friction. Fundamentally, it must now solve the inverse forms of the dynamic equations (i.e., a state-prescribed system), which are often more poorly conditioned than those that can be expressed as systems with force inputs. The dead-banding approach described in Section 7.2 was developed to handle static friction related discontinuities in this case, and could be generalized to other models. However, while in this case this approximation is not expected to degrade simulation accuracy, this may not always be the case.

In a fully-coupled simulation, in which hydrodynamics can be solved simultaneously with PTO dynamics (e.g., WEC-Sim), with a force input used throughout. While cases with complex hydrodynamics may not be suitably modeled via the linear hydrodynamics available in WEC-Sim, in this case it may have simplified implementation without substantially degrading accuracy.

These difficulties resulted in several deviations from test plan.

1. The highly non-linear nature of the system greatly complicated the construction of the feedback model, substantially increased computational time/cost, and prohibited accurate simplification that would have facilitated established workflows (e.g. *WecOptTool*).

2. At-sea testing was significantly delayed: it is not possible to use this data for model refinements.

# 8 Conclusions and Recommendations

The provided PTO model was incorporated with a linearized hydrodynamic model from ORCAFLEX simulation results to provide a fully-coupled closed-loop model for controls investigations. Linear systems describing device intrinsic impedance, PTO dynamics, and wave excitation were derived to facilitate this simulation. Models of three different levels of fidelity were produced, a wholly linear frequency-domain model, a nearly-linear time-domain model, and full model including a simplified version of the component-level PTO. Control investigations suggest that the motor approaches saturation limits operating under optimal gain combinations. In the sea-states of interest, the addition of a reactive integral controller offers minor improvement to power capture, but may provide more significant benefit in other sea-states. The benefit of an integral term predicted to be more significant if mechanical power is the target of optimization. Frequency-domain models suggest that more significant power capture improvement may be possible through use of a controller with non-zero cross coupling terms, though improvements in power capture were not observed to be as significant as the frequency-domain model suggests on the full-system model. Additionally, the linearized time domain model was found to be an especially poor predictor of full-system performance for

the cross-coupled controller. Significant static friction in the pumps is recommended as an area of particular design improvement, along with re-considering the accumulator recharge logic. Torque saturation limits on the generator do have an effect, but are not as significant as a limitation on instantaneous power: the ability to maintain torques suggested by optimal controller gain configurations for short (<1 seconds) so that power can greatly exceed the 35 KW rating is predicted to substantially improve power capture.

For the best available full system model, the optimal damping controller was found to perform well in all sea states, with a symmetric simplified cross-coupled controller providing a 2% increase in power capture in sea-states 2 and 3. Compared to the originally implemented controller, this suggests that the most significant performance enhancement investigated would be allowing the bow, starboard, and port gains to be unique. Or at a minimum, allowing the bow gain to be distinct from the starboard and port gains, which showed nearly identical optima in all investigated cases. This implies, however, that either the optimal tuning will become a stronger function of wave direction, or the mooring system should be designed to yaw in such a way that the designated 'bow' power-take-off is the first to encounter the exciting wave train.

## Bibliography

[1] R. G. Coe, G. Bacelli, and D. Forbush, "A practical approach to wave energy modeling and control," *Renewable and Sustainable Energy Reviews (submitted)*, 9 2020. [Online]. Available: https://www.techrxiv.org/articles/preprint/A_practical_approach_to_wave_energy_modeling_and_control/12939488

[2] G. Bacelli and R. G. Coe, "Comments on control of wave energy converters," *IEEE Transaction on Control System Technologies*, pp. 1–4, February 2020. [Online]. Available: https://ieeexplore.ieee.org/document/9005201

[3] R. G. Coe, G. Bacelli, S. J. Spencer, D. Forbush, and K. Dullea, "Advanced WEC dynamics and controls MASK3 test," Sandia National Laboratories, Tech. Rep. SAND2019-15428, 2019. [Online]. Available: https://doi.org/10.2172/1592850

[4] R. G. Coe, G. Bacelli, S. J. Spencer, and H. Cho, "Initial results from wave tank test of closed-loop WEC control," Sandia National Laboratories, Albuquerque, NM, Tech. Rep. SAND2018-12858, 2018. [Online]. Available: https://doi.org/10.2172/1531328

[5] D. D. Forbush, G. Bacelli, S. J. Spencer, and R. G. Coe, "A self-tuning WEC controller for changing sea states (in press)," in *Proceedings of the 21st IFAC World Congress*, 2020.

[6] H. Cho, G. Bacelli, and R. G. Coe, "Model predictive control tuning by inverse matching for a wave energy converter," *Energies*, vol. 12, no. 21, p. 4158, Oct 2019. [Online]. Available: http://dx.doi.org/10.3390/en12214158

[7] G. Bacelli, R. G. Coe, D. Patterson, and D. Wilson, "System identification of a heaving point absorber: Design of experiment and device modeling," *Energies*, vol. 10, no. 10, p. 472, 2017. [Online]. Available: http://www.mdpi.com/1996-1073/10/4/472

## 9 Acknowledgments

Sandia National Laboratories is a multi-mission laboratory managed and operated by National Technology and Engineering Solutions of Sandia, LLC., a wholly owned subsidiary of Honeywell International, Inc., for the U.S. Department of Energy's National Nuclear Security Administration under contract DE-NA0003525. This paper describes objective technical results and analysis. Any subjective views or opinions that might be expressed in the paper do not necessarily represent the views of the U.S. Department of Energy or the United States Government.

## 10 Appendix

### 1.14.2.5 Partial load efficiency of S120 Motor Modules

The charts below show the partial-load efficiency of air-cooled SINAMICS S120 Motor Modules for constant-torque drives. The calculations are based on a typical efficiency at full load of 98.5 %. The efficiency is represented in two different ways. In one chart, the efficiency is shown as a function of the output frequency with the output current as a parameter, and in the second chart, as a function of the output current with the output frequency as a parameter.

Figure 1a) shows the characteristic curve of the efficiency for constant-torque drives as a function of the output frequency ratio $f_{Out}/f_{Out\text{-}rated}$ which is proportional to the motor speed ratio $n/n_{rated}$. The parameter for the family of curves is the output current ratio $I_{Out}/I_{Out\text{-}rated}$ which is proportional to the motor torque ratio $M/M_{rated}$.

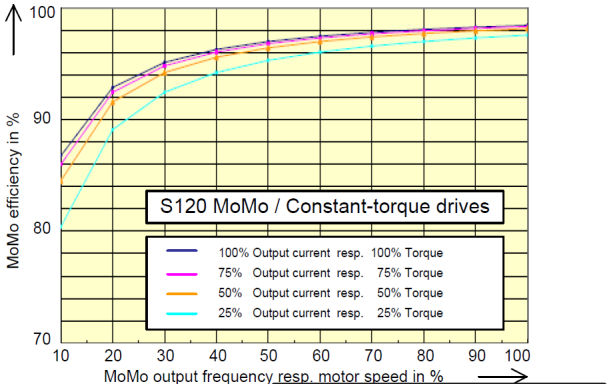



Figure 49: Drive efficiency as a function of motor speed, provided by OPI.

Figure 1b) shows the characteristic curve of the efficiency for constant-torque drives as a function of the output current ratio $I_{Out}/I_{Out\text{-}rated}$ which is proportional to the motor torque ratio $M/M_{rated}$. The parameter for the family of curves is the output frequency ratio $f_{Out}/f_{Out\text{-}rated}$ which is proportional to the motor speed ratio $n/n_{rated}$.

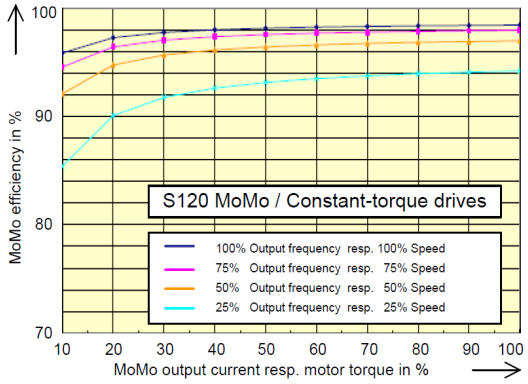



**Figure 1b)**
**Efficiency of air-cooled SINAMICS S120 Motor Modules in constant-torque drives as a function of the output current ratio in %**

Figure 50: Drive efficiency as a function of motor torque, provided by OPI.